μSR STUDIES OF HIGH-TC SUPERCONDUCTORS:
EFFECT OF VORTEX LATTICE DISORDER ON TF-μSR MEASUREMENTS OF THE MAGNETIC PENETRATION DEPTH AND NUCLEAR CONTRIBUTION TO THE ZF-μSR RELAXATION SPECTRUM

by

Wen Huang

B.Sc., South China University of Technology, 2009

Thesis Submitted in Partial Fulfillment
of the Requirements for the Degree of
Master of Science

IN THE
DEPARTMENT OF PHYSICS
FACULTY OF SCIENCE

SIMON FRASER UNIVERSITY

Summer 2011

APPROVAL

Name: Wen Huang

Degree: Master of Science

Title of Thesis: μSR Studies of High-T_c Superconductors: Effect of Vortex Lattice Disorder on TF-μSR Measurements of the Magnetic Penetration Depth and Nuclear Contribution to the ZF-μSR Relaxation Spectrum

Examining Committee: Dr. J. Steven Dodge (Chair)

Dr. Jeff Sonier, Senior Supervisor
Professor, Department of Physics

Dr. Malcolm Kennett, Supervisor
Assistant Professor, Department of Physics

Dr. David Broun, Supervisor
Associate Professor, Department of Physics

Dr. Daniel B. Leznoff, Internal Examiner
Professor, Department of Chemistry

Date Approved: 18 August 2011

Declaration of
Partial Copyright Licence

Abstract

Muon Spin Rotation/Relaxation (μSR) is an experimental technique widely used to probe magnetism in high-temperature (high-T_c) superconductors. This thesis consists of two distinct μSR studies of high-T_c materials: namely, transverse-field (TF) μSR measurements of the iron-arsenic superconductor $BaFe_{2-x}Co_xAs_2$ and a zero-field (ZF) μSR investigation of the cuprate superconductor $La_{2-x}Sr_xCuO_4$ (LSCO).

A model for severe random frozen disorder of the vortex lattice in $BaFe_{2-x}Co_xAs_2$ is developed and used to explain limitations imposed on TF-μSR measurements of the superconducting magnetic penetration depth in doped iron-arsenic superconductors. In the latter part of the thesis, ZF-μSR measurements on LSCO show no evidence for spontaneous magnetic order in the pseudogap regime. Instead, experiments suggest that the random nuclear dipole moments are the dominant contribution to the ZF-μSR relaxation. To determine the exact form of the nuclear contribution to the ZF-μSR signal, the nuclear contribution is modeled quantum mechanically and compared to the experimental results.

To my beloved Mom

Acknowledgments

First of all I owe my deepest gratitude to Prof. Jeff Sonier, who has patiently guided me through two years of research. This thesis would not have been possible without the encouragement and support from Jeff. It has been a great honor for me to be Jeff's student. I am also grateful to the faculty members who taught the courses I have taken and audited during my Master's study. I would also like to thank my colleagues and office mates Christina Kaiser, Zahra Lotfi and Gabe Scholz, with whom I did the experiments, shared the lab space and many funny stories. In particular, I thank Christina for explaining to me many things that I did not know before, and for having many extremely useful discussions on our researches. I would also like to show my gratitude to my friend Xiao-Li Huang for providing a time-saving (or maybe life-saving) computing code used in my thesis research and for having many valuable discussions with me. I am also indebted to Vighen Pacradouni, a past member of our research group who initiated one of the projects of my research, though I had met him only twice. Also, though their names are not listed here, I would like to thank many students and friends in the Physics Department for their friendship and kindness which have made my stay in Vancouver and at SFU an unforgettable experience. Last but most importantly, I thank my parents and siblings who have always been a lasting source of moral support and encouragement, and thank Chiao-Ling Shen for her deeply treasured companionship during the formation of this thesis.

Contents

List of Tables

List of Figures

Chapter 1

Introduction

Muon Spin Rotation/Relaxation (μSR) is an experimental technique that has been widely used to probe magnetism in various materials. This thesis consists of two separate μSR studies of high transition-temperature (T_c) superconductors, namely, transverse-field (TF) μSR measurements of the iron-arsenic superconductor $BaFe_{2-x}Co_xAs_2$ and a zero-field (ZF) μSR investigation of the cuprate superconductor $La_{2-x}Sr_xCuO_4$. Some of the basic properties of these materials that are relevant to this thesis are introduced in this chapter.

1.1 Basic Magnetic Response of Superconductors

The TF-μSR measurements are performed with an external magnetic field applied to the sample, which necessiates a basic understanding of the generic magnetic response of superconductors. In weak magnetic fields superconductors exhibit perfect diamagnetism via persistent screening electrical currents near the surface. These so-called "supercurrents" generate a magnetic field which completely cancels the applied magnetic field in the sample interior, except near the surface where the supercurrents reside. This diamagnetic response is known as the "Meissner effect". In type-I superconductors, the Meissner effect occurs below a critical applied field $H_c(T)$, above which magnetic flux fully penetrates the bulk of the sample (see Fig. 1.1(a)). In type-II superconductors the Meissner effect occurs below a critical field $H_{c1}(T)$, above which the material responds to stronger external field by allowing partial penetration of quantized magnetic flux in the form of a lattice of "vortices". Each vortex is comprised of circulating supercurrents surrounding a magnetic flux quan-

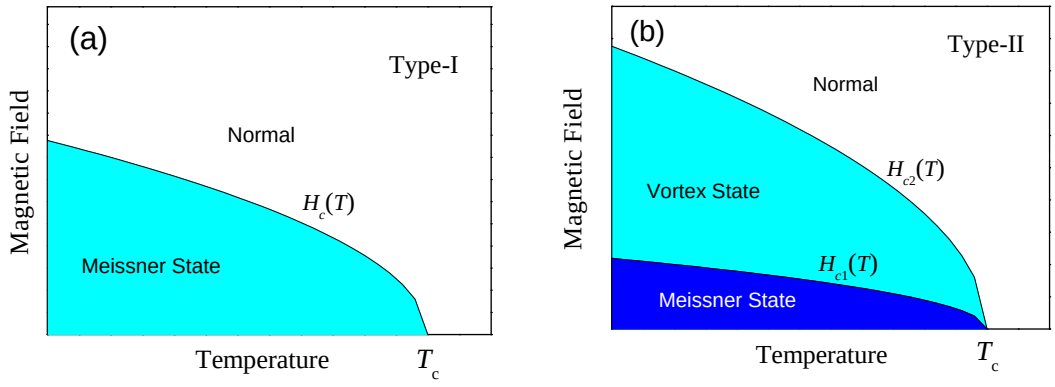

Figure 1.1: Magnetic phase diagram showing the generic response of (a) type-I and (b) type-II superconductors to an applied magnetic field.

tum $\phi_o = hc/2e$. For applied fields greater than an upper critical field $H_{c2}(T)$, the material reverts back to the normal state with magnetic flux fully penetrating the sample interior. Figure 1.1(b) shows the generic magnetic phase diagram of a type-II superconductor.

The size of the vortex cores near H_{c2} is roughly the size of the Ginzburg-Landau (GL) coherence length ξ [1], which is defined as the length scale for spatial variations of the superconducting order parameter, $\Delta(r)$. As shown in Fig. 1.2, $\Delta(r=0)=0$ at the centre of the vortex core and rises to its maximum value far from the core centre; where in the case of an isolated vortex full superconductivity is restored. The magnetic field decays outside the vortex cores in an exponential-like manner on the length scale of the magnetic penetration depth λ (see Fig. 1.2). In London theory, which is based on Maxwell's equations, λ is given by [2]

$$\frac{1}{\lambda^2} = \frac{4\pi^2 n_s e^2}{m^* c^2}, \tag{1.1}$$

where n_s and m^* are the density and effective mass of the superconducting carriers, respectively. The superconducting carriers are formally known as "Cooper pairs", which are bound pairs of electrons that have opposite spin and momentum ($\hbar\mathbf{k}$ and -$\hbar\mathbf{k}$) in the vicinity of the Fermi surface. In the Bardeen-Cooper-Schrieffer (BCS) theory [3], the pairing arises from an effective attractive pairwise interaction of electrons, which in conventional

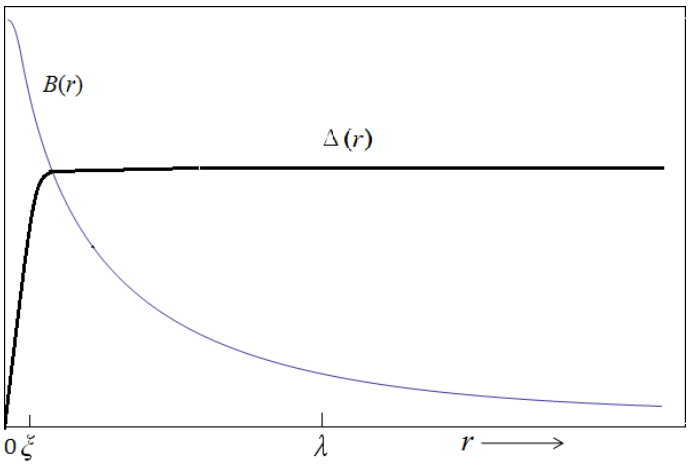

Figure 1.2: The superconducting order parameter $\Delta(r)$ and the spatial dependence of the magnetic field $B(r)$ of an isolated vortex, where r is the distance from the vortex centre.

low-T_c superconductors is mediated by phonons. The minimum energy of the quasiparticle excitation (*i.e.* the minimum energy required to break the Cooper pair) is known as the superconducting pairing gap $\Delta_{\mathbf{k}}$. The $\mathbf{k}$-space dependence of the energy gap reflects the symmetry of the pairing state (*i.e.* *s*-wave, *d*-wave, *p*-wave etc.). Conventional superconductors that are explained by the BCS theory have *s*-wave pairing.

According to Eq. (1.1), n_s may be inferred from measurements of the magnetic penetration depth λ. With increasing temperature, Cooper pair breaking leads to a reduction of n_s. Hence λ increases with increasing T and at $T = T_c$, $\lambda \to \infty$; corresponding to complete magnetic flux penetration.

The symmetry of the pairing gap can be inferred from the temperature dependence of λ. In conventional *s*-wave superconductors where the pairing gap is isotropic and nonzero everywhere, (*i.e.* $\Delta_{\mathbf{k}} \equiv \Delta_o$), the number of quasiparticle excitations is exponentially small at $T \ll T_c$. Specifically the BCS theory predicts that at low temperatures the T-dependence of λ is expressed as [4]

$$\frac{\Delta\lambda(T)}{\lambda(0)} \approx 3.33 \left(\frac{T}{T_c}\right)^{1/2} \exp(-1.76 T_c/T)\,. \tag{1.2}$$

If there exist line or point nodes (*i.e.* $\Delta_{\mathbf{k}} = 0$ for certain $\mathbf{k}$) in the pairing gap function $\Delta_{\mathbf{k}}$, low energy quasiparticle excitations can be significant even at $T \ll T_c$, giving rise to power-

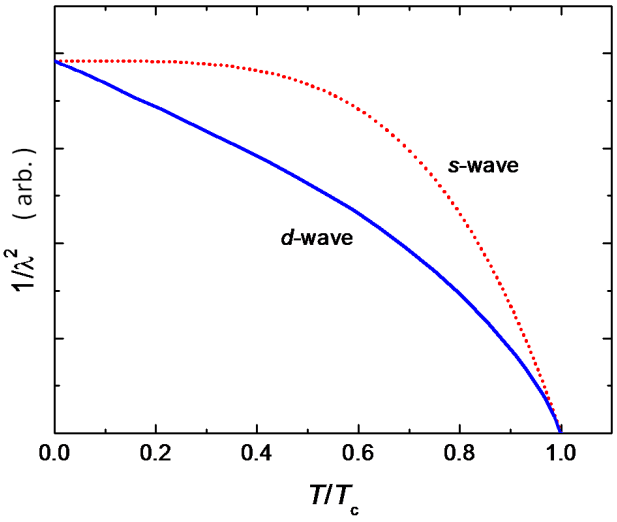

Figure 1.3: Plot of the temperature dependence of the magnetic penetration depth λ for s-wave and d-wave pairing symmetries. Note that the weak exponentially-activated temperature dependence of $1/\lambda^2$ at low T for a fully-gapped s-wave superconductor is distinct from the strong limiting low-T linear temperature dependence of a nodal d-wave superconductor.

law behaviour $\Delta\lambda(T) \propto T^n$, n=1, 2, 3, or 4 [5]. In particular, $\lambda(T) \sim \lambda(0)[1+\ln 2(T/\Delta_o)]$ is the expected limiting low-temperature behaviour for a pure d-wave superconductor [6], which has a gap function of the form $\Delta_o(\cos k_x + \cos k_y)$, where Δ_o is the gap maximum. This is the situation for high-T_c cuprate superconductors, which are discussed in the next section. The linear-T dependence of λ in cuprate superconductors has been confirmed by TF-μSR measurements in the vortex state as well as other techniques that measure λ or $\Delta\lambda = \lambda(T) - \lambda(0)$ in the Meissner state, such as a microwave cavity perturbation [7]. Figure 1.3 shows examples of the temperature dependence of $1/\lambda^2$ expected for s-wave and d-wave superconductors, which according to Eq. (1.1) is proportional to the superconducting carrier density n_s.

1.2 Cuprate Superconductors

Following the discovery of high-T_c superconductivity in $La_{2-x}Ba_xCuO_4$ in 1986 [8], cuprate superconductors have been under intense investigation aimed at deducing the microscopic mechanism responsible for superconductivity in these materials. The cuprates are characterized by a layered structure consisting of CuO_2 planes, where the Cu atoms form a square lattice. Although conventional band theory predicts them to be metallic, due to strong Coulomb interaction of the electrons, the parent compounds of the cuprates (*e.g.* La_2CuO_4) are insulators, with the electrons localized at the Cu atoms in the d^9 electronic configuration and the associated Cu moments exhibiting long-range antiferromagnetic (AFM) order. Many of the cuprates, including La_2CuO_4 can be chemically doped by cation substitution. In La_2CuO_4, substitution of some of the trivalent La by divalent Sr introduces x hole carriers into the CuO_2 planes of the resultant $La_{2-x}Sr_xCuO_4$ (LSCO). Figure 1.4 shows the basic phase diagram of hole-doped cuprates. Some cuprates can instead be doped with electrons [9], but these are not discussed here. In $La_{2-x}Sr_xCuO_4$, the hole concentration is equivalent to the Sr content x. The long-range AFM order of the La_2CuO_4 is rapidly destroyed with increased doping, giving way to short-range static magnetic (SM) order that persists to about $x = 0.13$ [10, 11]. Beyond $x \sim 0.05$ and below $x \sim 0.27$, superconductivity occurs. The phase diagram of Fig. 1.4 is characterized by a superconducting "dome", where T_c first increases with increased doping, but decreases beyond an optimal non-universal value of T_c. For LSCO, the optimal doping is at $x \sim 0.16$. The superconducting region to the left of optimal doping is referred to as the "underdoped" region, while that to the right is dubbed the "overdoped" region. This doping dependence of T_c is universal to all cuprates. It is generally agreed that superconductivity in doped cuprates cannot be explained by a BCS theory for d-wave superconductors. The proximity of the superconducting and AFM phases and the persistence of AFM fluctuations to the high-doping edge of the superconducting dome [12] have contributed to the general belief that the mechanism for high-T_c superconductivity is magnetic in origin.

A distinctive feature of the cuprate superconductors is an energy gap near the Fermi surface in momentum space that exists above the superconducting dome in the underdoped region. This is referred to as the "pseudogap". In contrast to the superconducting gap, the pseudogap does not appear to be directly related to bulk superconductivity, as the pseu-

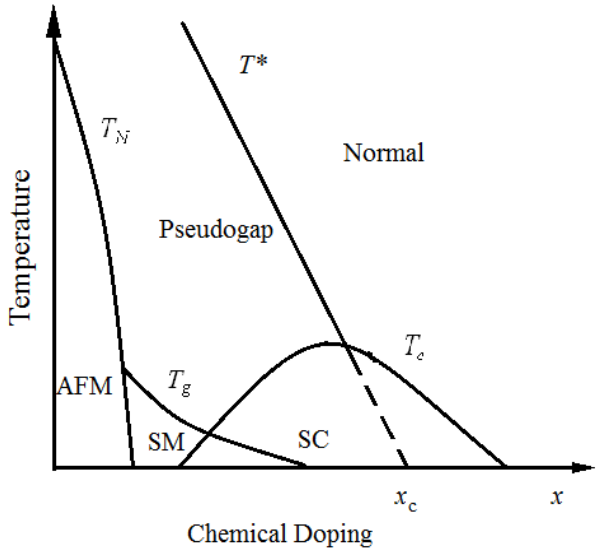

Figure 1.4: Basic phase diagram of hole-doped cuprate superconductors. The introduction of charge carriers quickly suppresses the long-range antiferromagnetic (AFM) order of the insulating parent compounds, giving rise to short-range static magnetic (SM) order. A superconducting (SC) phase appears at higher dopings. The T^* curve indicates the crossover into the pseudogap region. Its extension below T_c (indicated as a dashed curve), terminating at a quantum critical point x_c, is somewhat speculative.

dogap temperature T^* decreases linearly as a function of hole doping. Various theories have been proposed regarding the origin of the pseudogap, with some suggesting that it is a precursor of the superconducting gap, while others have argued that it is a signature of a competing ground state. An important issue of debate has been whether the pseudogap region is a thermodynamic phase, in which case a true phase transition occurs at T^*. In this scenario one or more symmetries are broken. One specific idea are proposals of time-reversal symmetry breaking phases that contain ordered circulating orbital currents, where pairs of electron loop currents flow in the O-Cu-O plaquettes in the CuO_2 plane (See Fig. 1.5) [13, 14, 15, 16]. Among the proposed loop-current states, the so-called d-density wave (DDW) order breaks the translational symmetry of the lattice [13], while circulating-current (CC) order preserves the translational symmetry of the lattice [14, 15, 16]. In this picture, T^* marks a real phase transition to a state with long-range magnetic order due to the loop currents, and T^* vanishes at a quantum critical point x_c below the superconducting dome. Recently, an abrupt onset of an energy gap at T^* above the superconducting transition has been observed in the nearly optimally doped cuperate superconductor $Pb_{0.55}Bi_{1.5}Sr_{1.6}La_{0.4}CuO_{6+\sigma}$ by the combined techniques of angle-resolved photoemission spectroscopy (ARPES), the polar Kerr effect and time-resolved reflectivity, indicating a real phase transition at T^* [35].

The existence of a loop-current phase in cuprates is supported by several measurements in the pseudogap region. Unusual weak magnetic orders have been detected in $YBa_2Cu_3O_y$ (YBCO) [18, 19, 20, 21, 22, 23], $HgBa_2CuO_{4+\delta}$ (Hg1201) [24] and $La_{1.915}Sr_{0.085}CuO_4$ [25] by neutron scattering that bear some resemblance to the predicted loop-current orders. In particular, two kinds of magnetic order were seen in YBCO by neutrons. One breaks the translational symmetry [18, 19, 20], with an onset of magnetic order at roughly T^*, but with weak magnetic moments that are smaller than 0.05 μ_B. The other, which has been observed by polarized neutron scattering, preserves the translational symmetry [21, 22, 23], with an onset temperature that tracks T^* at a function of hole doping. This second type of unusual magnetic order is three-dimensional (3D) and long-range ordered. It has also been observed in Hg1201 [24], which like YBCO is hole-doped via changes in oxygen content. Similar magnetic order has also been seen by polarized neutrons in $La_{1.915}Sr_{0.085}CuO_4$ [25], but it is instead 2D and short range. Additional evidence for loop-current order is circular dichroism observed in $Bi_2Sr_2CaCu_2O_{8+\delta}$ by ARPES measurements, indicative of a phase

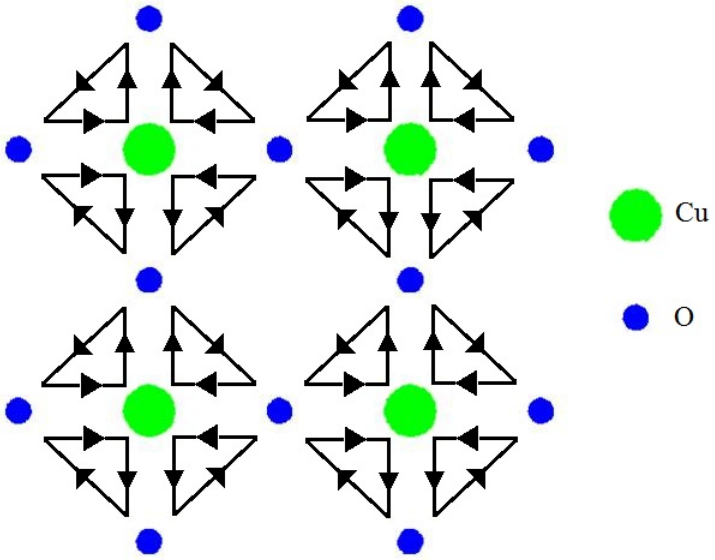

Figure 1.5: Diagram of a proposed loop-current pattern in the CuO_2 plane, which preserves translational symmetry [15, 16].

of broken time reversal symmetry [26]. However, this measurement is highly disputed, with some arguing that circular dichroism might instead result from distortions and modulations of the crystal lattice as temperature is varied [27]. Weak ferromagnetism in the pseudogap region has also been detected in YBCO by high-resolution polar Kerr effect experiments [28]. Such a ferromagnetic order is argued to be compatible with the CC phase when inversion symmetry of the crystal is also broken [29]. Finally, bulk susceptibility measurements observed a non-analytical variation of the temperature derivative of the susceptibility in underdoped polycrystalline YBCO samples, providing further evidence for a true phase transition near T^* [30].

1.3 Search for Loop-Current Order by ZF-μSR

Despite the above experimental evidence for a loop-current phase, local magnetic probes, such as zero-field muon spin relaxation (ZF-μSR) and nuclear magnetic resonance (NMR) have so far failed to observe the onset of magnetic order in the pseudogap region. This is suprising given the high sensitivity of these methods to local magnetic order. In contrast

to the other experimental techniques mentioned above, the local probe methods enable a determination of the magnetic volume fraction. This is important, since the interpretation of the pseudogap region as a phase of loop-current order requires that the magnetic order exist throughout the sample.

While an early ZF-μSR study of high-quality YBCO single crystals revealed weak static magnetism in the pseudogap region [31], it was later shown that the observed magnetism is most likely caused by the CuO chains and structural changes that are unique to YBCO [32]. This interpretation is consistent with a recent ZF-μSR study [36], which indicates that the magnetism detected in the earlier experiments is the same unexplained weak translational-symmetry breaking magnetic order detected in $YBa_2Cu_3O_{6.6}$ by neutron scattering experiments [18]. The onset temperature of this kind of weak magnetic order does not change with hole-doping concentration and hence is clearly uncorrelated with T^* and unrelated to the pseudogap.

It is unclear whether the magnetic order that preserves translational symmetry, which has been observed by polarized neutron scattering in the pseudogap region of YBCO [21, 22, 23], Hg1201 [24] and LSCO [25] is the loop-current order of the proposed CC phase. This second kind of weak magnetic order has an ordered moment with a large component in the CuO_2 plane. This large in-plane component requires modification of the original CC theory to explain [33, 34, 35]. Moreover, neutron experiments say nothing about the volume fraction of this magnetic order. A ZF-μSR study [36] of the same $YBa_2Cu_3O_{6.6}$ single crystal measured by polarized neutron scattering in Ref. [22] suggests that this unusual magnetic order exists in only $\sim 3\%$ of the sample. The evidence that the static magnetic order detected by ZF-μSR is the second unusual type of weak magnetism comes from the observation that local magnetic field detected by the muons is in good agreement with the magnetic arrangement and ordered moment deduced from the neutron scattering experiments. A further challenge to the interpretation of the polarized neutron measurements as support for CC model is that this second kind of unusual magnetic order was not observed by ZF-μSR in higher-quality YBCO single crystals [36].

To reconcile the discrepancy between the ZF-μSR and polarized neutron scattering results, it has been suggested that charge screening of the positively charged muon severely perturbs the local environment, causing the loop-current order to vanish over several lattice constants [37]. However, this assertion contradicts the excellent agreement that ex-

ists between ZF-μSR and (non-perturbative) NMR measurements of the onset temperature for long-range and short-range static magnetic order in underdoped LSCO [10] (See regions labeled AFM and SM in Fig. 1.4). Moreover, a recent ^{89}Y NMR experiment on $Y_2Ba_4Cu_7O_{15-\delta}$ [38] and a Zeeman perturbed nuclear quadrupole resonance (NQR) study of powdered samples of $YBa_2Cu_4O_8$ [39] have failed to detect either of the unusual magnetic orders mentioned above.

A recent ZF-μSR study of single crystals of LSCO over a wide doping range ($x = 0.13,\ 0.19,\ 0.30$) [40] showed no evidence for loop-current order. The observed ZF-μSR spectra have relaxation rates that do not show an appreciable temperature dependence, consistent with what is expected for a relaxation dominated by randomly oriented nuclear magnetic moments. Furthermore, the ZF-μSR spectra at different dopings, but the same temperature, are nearly identical. This puts an upper limit of ~ 0.02 G for additional sources of local magnetic field sensed by the muon, which is several orders of magnitude smaller than the magnetic field generated by the proposed loop currents. Although this conclusion was reached with great confidence in Ref. [40], the ZF-μSR spectra cannot be described by the standard relaxation function commonly used for approximating the contribution of the randomly oriented nuclear dipole fields [41] (*i.e.* a Static Gaussian Kubo-Toyabe function). Consequently, the functional form of the ZF-μSR spectra of LSCO has not yet been fully described. In addition, the data collected in Ref. [40] was insufficient to conclude whether a small volume fraction ($\approx$ 3%) of the sample contained weak static magnetic order.

To address these issues, high precision ZF-μSR measurements on LSCO single crystals were carried out and are presented here. These findings corroborate the ZF-μSR study of Ref. [40]. In addition, the contributions of the random nuclear dipole moments to the ZF-μSR relaxation rate are modeled quantum mechanically and compared to the experimental results.

1.4 Iron-Arsenic Superconductors

A new family of high-T_c superconductors containing iron-arsenic layers was discovered in 2008 [42] (*e.g.* $LaFeAsO_{1-x}F_x$, $Ba_{1-x}K_xFe_2As_2$, $BaFe_{2-x}Co_xAs_2$). Like the high-T_c cuprate superconductors, the parent compounds of these newer superconductors are anti-

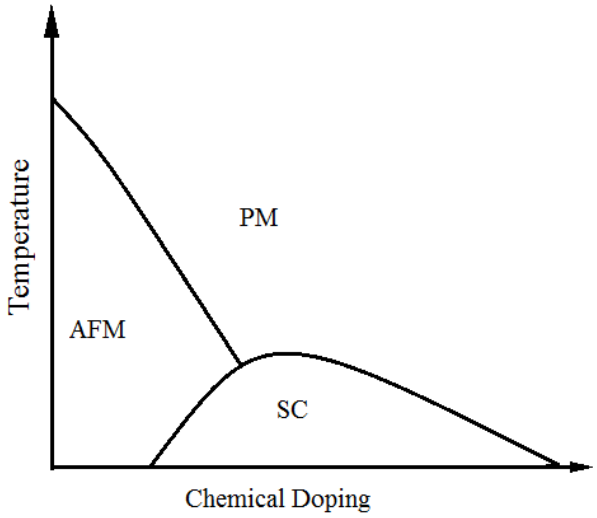

Figure 1.6: Generic doping phase diagram of iron-arsenic superconductors. As in the cuprates antiferromagnetic (AFM) order of the parent compound is quickly suppressed with increased chemical doping of charge carriers. Superconductivity (SC) sets in at higher dopings, exhibiting a superconducting dome. At higher temperatures, these compounds are paramagnetic (PM) metals.

ferromagnetic (AFM) with ordered moments on the square Fe sublattice [43, 44]. Also like the cuprates, the parent compounds are driven from AFM to superconducting by chemical doping that introduces charge carriers. Figure 1.6 shows the generic doping phase diagram of the iron-arsenic compounds, which exhibit AFM order at low doping and a superconducting dome at higher dopings. Note that although indicated in some measurements [45], unlike in cuprates, the existence of a pseudogap in iron-arsenic superconductors has not been firmly established.

Experiments thus far suggest that superconductivity in the iron-arsenic superconductors involves unconventional pairing, yet the symmetry of the pairing remains unclear. A typical example is the experimental effort to identify the pairing symmetry of electron-doped $BaFe_{2-x}Co_xAs_2$. Thermal conductivity measurements [46] suggest a nodeless superconducting gap which evolves from isotropic *s*-wave in low-doped samples to highly anisotropic in overdoped samples. A nodeless and isotropic *s*-wave gap was also observed in ARPES measurements on optimally doped $BaFe_{1.85}Co_{0.15}As_2$ [47]. Specific heat stud-

ies [49], however, indicate an isotropic gap that has no doping dependence, and optical conductivity measurements on overdoped $BaFe_{1.8}Co_{0.2}As_2$ [48] support the existence of two distinct energy gaps; a small isotropic gap and a larger highly anisotropic gap with possible nodes on different Fermi surfaces. This two-gap scenario is consistent with thermal conductivity measurements of an overdoped $BaFe_{1.73}Co_{0.27}As_2$ single crystal [50], and also with direct magnetic penetration depth measurements of $BaFe_{2-x}Co_xAs_2$ near optimal doping, via a mutual inductance method [51].

The TF-μSR obtains information on the superconducting pairing symmetry by deducing the temperature dependence of the magnetic penetration depth λ in the vortex state [52]. Note both the high-T_c cuprates and the high T_c iron-arsenides are type-II superconductors. Thus far this kind of measurements has been performed on polycrystalline and powdered samples, as well as single crystals of numerous iron-arsenic compounds. An early study of polycrystalline samples of $LaFeAsO_{1-x}F_x$ with $x = 0.075$ and $x = 0.10$ deduced a temperature dependence of λ that is consistent with both an *s*-wave and a dirty *d*-wave pairing [53]. In contrast, TF-μSR measurements on sintered powders of $SmFeAsO_{0.85}$ and $NdFeAsO_{0.85}$ indicate either the existence of an energy gap with nodes at the Fermi surface or two distinct superconducting gaps [54]. Single crystal measurements so far favour the two-gap scenario. TF-μSR measurements on single crystals of overdoped $SrFe_{1.75}Co_{0.25}As_2$ [55] and $Ba_{1-x}K_xFe_2As_2$ [56] both suggest two-gap superconductivity, as does measurements on the underdoped $BaFe_{1.86}Co_{0.14}As_2$ [57] that indicate the existence of two distinct *s*-wave superconducting gaps. However, TF-μSR studies of optimally doped and overdoped $BaFe_{2-x}Co_xAs_2$ and $SrFe_{2-x}Co_xAs_2$ single crystals [58] imply that the smaller gap is highly anisotropic (with possible nodes) in the higher doped region. In addition, TF-μSR measurements have revealed field-induced magnetic order in both $SrFe_{1.75}Co_{0.25}As_2$ and $BaFe_{2-x}Co_xAs_2$ samples [55, 58].

In single crystal measurements, λ is generally obtained by fitting the TF-μSR spectra to a phenomenological model of the vortex lattice [52]. In doing so it is assumed that the vortex lattice is highly ordered, which is not the case if there are defects and/or chemical disorder that strongly "pin" vortices from their ideal positions in the vortex lattice. This occurs when the pinning force exerted on a vortex exceeds the natural electromagnetic repulsion between vortices. As it turns out, many of the iron-arsenic superconductors exihibit highly disordered vortex lattices. Small-angle neutron scattering (SANS), magnetic

force microscopy (MFM) and Bitter decoration experiments on the doped KFeAs($O_{1-x}F_x$), $A_{1-x}B_x$Fe$_2$As$_2$ and AFe$_{2-x}$Co$_x$As$_2$ compounds show only highly disordered vortex lattices indicative of strong pinning [59, 60, 61, 62, 63, 64, 65]. Such a high degree of vortex-lattice disorder is problematic for an accurate analysis of the TF-μSR measurements. Yet the effects of severe disorder has not been considered in the interpretation of the TF-μSR studies mentioned above.

To clarify the effect of vortex-lattice disorder on TF-μSR measurements of this kind, a TF-μSR experiment on an overdoped single crystal of BaFe$_{2-x}$Co$_x$As$_2$ is presented here. It is first shown that there is a significant contribution from the field-induced magnetic order that cannot be easily isolated from the effect of vortex-lattice disorder. Next, numerical simulations of highly disordered vortex lattices are presented and it is explained how vortex-lattice disorder affects an accurate determination of the magnetic penetration depth by TF-μSR, even in samples withouth field-induced magnetism.

Chapter 2

Experimental Methods: μSR

2.1 Introduction

Muon Spin Rotation/Relaxation/Resonance (μSR) is an experimental technique that utilizes spin-polarized muons to primarily probe magnetism in materials. Like the related method of NMR, μSR is a local probe sensitive to magnetic volume fractions and uncorrelated spins. However, μSR is more sensitive to weak magnetic moments, slow spin fluctuations, and/or dilute magnetism. It is especially suited for investigations of high transition-temperature (T_c) superconductors, where magnetism interplays extensively with superconductivity.

2.1.1 Muon Properties and Muon Decay

The muon is an elementary spin-1/2 particle with a mass approximately 200 times that of an electron, and carries a positive (μ^+) or negative charge (μ^-). The muon is an unstable particle, with a mean lifetime of $\tau_\mu \sim 2.2$ μs. The μ^+ (μ^-) spontaneously decays into a positron (electron) as follows

$$\begin{aligned} \mu^+ &\rightarrow e^+ + \nu_e + \bar{\nu}_\mu \\ \mu^- &\rightarrow e^- + \bar{\nu}_e + \nu_\mu \,. \end{aligned} \tag{2.1}$$

Because the μ^- behaves like a heavy electron in materials, it can be captured by a host nucleus to form a muonic atom in which the muon's orbital is ~ 200 times smaller than

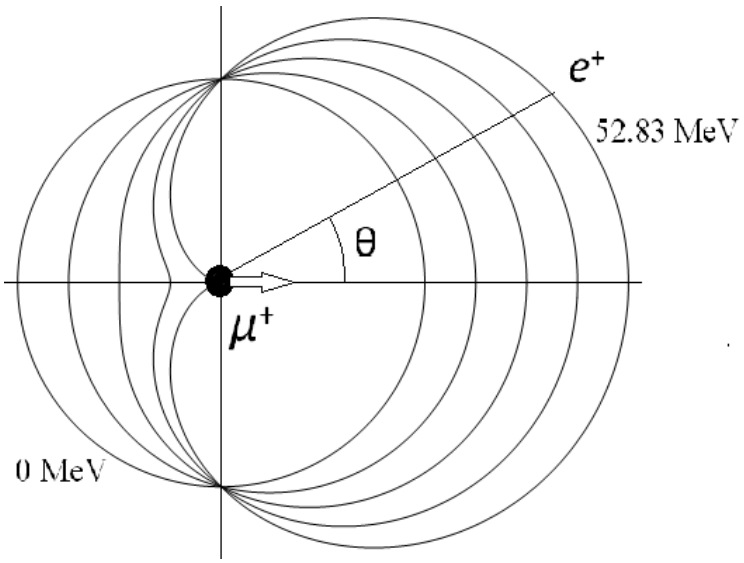

Figure 2.1: Angular distribution of positrons resulting from μ^+ decay for various positron kinetic energies. The horizontal arrow indicates the direction of the muon spin at the time of decay. θ is the angle between the muon spin and the direction of positron emission.

that of the corresponding electronic orbital. The muon spin information is lost through spin-changing transitions in the atomic cascade as the muon emits x-rays upon its transfer to the $1S$ ground state. Hence it is the μ^+ that is primarily used for studies of magnetism. When the μ^+ decays, a positron is preferentially emitted along the direction of the muon spin orientation according to the probability function

$$W(E,\theta) = 1 + a(E)\cos\theta, \tag{2.2}$$

where θ is the angle between the direction of the muon spin and the emitted positron, and a is an asymmetry parameter which increases monotonically with the positron kinetic energy. The positron kinetic energy is distributed between $E=0$ and $E=52.83$MeV. For the maximum positron energy, $a = 1$. If all positron energies are equally sampled, the effective probability function becomes $W(\theta) = 1 + \bar{a}\cos\theta$, with $\bar{a} = 1/3$. Figure 2.1 shows a polar diagram of the angular distribution of positrons for different decay kinetic energies.

The spin 1/2 of the muon makes μSR a pure magnetic probe. This is in contrast to NMR, where for nuclei with spin $I > 1/2$, one also has to deal with the coupling of the electric quadrupole moment of the nucleus to the local electric field gradient. The spin-1/2 μ^+ is

purely sensitive to the local magnetic environment of the material. With a gyromagnetic ratio of $\gamma_\mu = 851.616$ rad $\cdot$ MHz/T, the muon precesses about the local static or dynamic magnetic field **B** with a Larmor frequency $\omega_\mu = \gamma_\mu B$. One of the reasons that μSR is more sensitive to magnetism than NMR is that the magnetic moment of the muon is 3.18 times larger than that of the proton. The μSR method can be used to detect magnetic moments as small as $10^{-3}\mu_B$.

2.1.2 Production of Polarized Muon Beams

A nearly 100% spin polarized μ^+ beam is generated by exploiting the parity violating decay of positive pions

$$\pi^+ \rightarrow \mu^+ + \nu_\mu \,. \tag{2.3}$$

The π^+ are created from $\sim$500 MeV protons striking a primary production target (C or Be). The π^+ that come to rest on the downstream side of the production target decay according to Eq. (2.3). Conservation of linear momentum requires that the μ^+ and ν_μ are emitted in opposite directions. The π^+ has spin zero, and the helicity of the ν_μ is fixed at -1 (*i.e.* the ν_μ carries a spin that is in a direction opposite to its linear momentum). Conservation of both angular and linear momentum therefore requires that the spin of the μ^+ is also directed antiparallel to its own linear momentum. The μ^+ resulting from such a decay emerges isotropically from the π^+, with momentum $p_\mu = 29.8$ MeV/c and kinetic energy $E_k = 4.119$ MeV in the rest frame of the π^+. However, by collecting μ^+ emitted within a small solid angle from the primary production target, a nearly 100% spin polarized beam is achieved. This type of muon beam is called a "surface" muon beam, and is the most common type of μ^+ beam in modern μSR facilities. Higher momentum spin polarized μ^+ beams can be created via the decay of in-flight π^+ [66], and a low-energy (keV) μ^+ beam may be created using moderators [67], but with greatly reduced intensity. It is worth mentioning that the kinetic energy of the surface muon beam implies a mean stopping range of 140 mg/cm^2 in a targeted sample. Consequently, when surface muons are used, μSR is a local probe of the bulk.

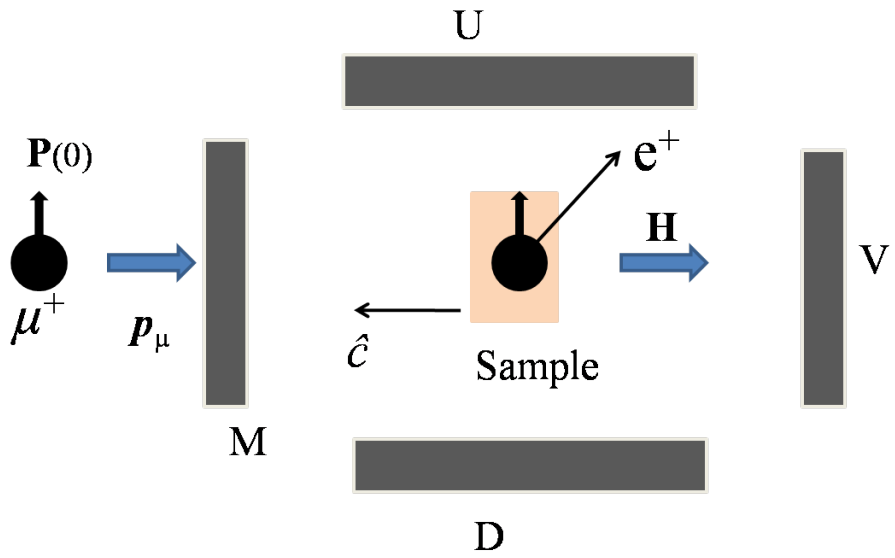

Figure 2.2: Configuration of the μSR experiments reported in this thesis. **H** is the external magnetic field used in some of the experiments. Detector M records the incoming muons. The veto (V) detector behind the sample suppresses the unwanted background signal from muons that do not stop in the sample. The asymmetry spectrum is obtained from decay positron counts in the up (U) and down (D) detectors. Note in the experiments where $H \neq 0$, additional positron detectors L and R were placed on either side of the sample (*i.e.* in and out of the page) to capture more of the decay positron solid angle.

2.1.3 Asymmetry Spectrum

Figure 2.2 shows a schematic of the primary configuration used in the μSR experiments reported in this thesis. The measurements were performed on surface muon beamlines M15 and M20 at TRIUMF. A Wien filter was used to rotate the spin of the incoming muons by 90°, resulting in an initial spin polarization $\mathbf{P}(0)$ perpendicular to the beam linear momentum $\mathbf{p}_\mu(0)$. At time $t=0$ a μ^+ passes through the muon scintillator detector (M), triggering an electronic clock. This instant is also considered to be the time when the μ^+ comes to rest in the sample, as the time it takes for the μ^+ to travel from detector M to the sample is negligible. A veto (V) detector placed behind the sample is used to exclude muons that miss or pass through the sample. As time progresses, other muons passing through M are electronically excluded until the decay positron of the μ^+ is detected by the U or D scintillator detectors placed around the sample. Hence, ideally there is only one μ^+ stopped in the sample at a time. The clock is stopped at time t when a positron event is detected. After the implantation of millions of μ^+, one obtains a histogram consisting of the number of decay events as a function of the time the μ^+ spent in the sample. The "asymmetry spectrum" is defined as

$$A(t) = \frac{[N_+(t) - B_+] - [N_-(t) - B_-]}{[N_+(t) - B_+] + [N_-(t) - B_-]}, \tag{2.4}$$

where $N_\pm(t)$ are the time histograms of the positron counts recorded in the two detectors (*i.e.* U and D) and $B_\pm$ are the time independent random backgrounds due to numerous sources. The time histograms of the positron detectors $N_\pm(t)$ are defined as follows

$$N_\pm(t) = N_{o\pm} \exp(-t/\tau_\mu)[1 \pm a_o P(t)] + B_\pm . \tag{2.5}$$

Here $P(t)$ is the time evolution of the muon spin polarization, $N_{o\pm}$ is a $t=0$ normalization constant for the positron counts, the exponentially decaying term accounts for the finite life time of the muon, and a_o is the initial asymmetry. Ideally, $a_o = \bar{a} = 1/3$, which is associated with the positron emission probability distribution Eq. (2.2). However, in real measurements a_o is typically smaller than 1/3, due to various experimental conditions, such as the range of positron kinetic energies which are detected and the solid angle of the detectors. Assuming identical positron detectors and substituting Eq. (2.5) into Eq. (2.4),

the asymmetry spectrum is related to $P(t)$ as follows

$$A(t) = a_{\mathrm{o}} P(t)\,. \tag{2.6}$$

Note that there are more general relations that relate $A(t)$ to $P(t)$ when there are differences in positron detector efficiency and/or counter misalignments.

The μSR methods can be applied in the presence or absence of an external magnetic field. The latter is possible because unlike NMR an applied magnetic field is not required to create the initial muon spin polarization. Figure 2.3 shows simulations of $N_{\pm}(t)$ for two opposing positron detectors and for two different experimental configurations, together with the associated asymmetry $A(t)$. The two different experimental configurations used for this thesis (*i.e.* zero-field (ZF) and transverse-field (TF) μSR), are discussed next.

2.2 ZF-μSR

Zero-field (ZF) μSR is particularly useful for probing weak magnetism in the bulk of samples. For zero external magnetic field, the effective magnetic field acting on the muon spin is the vector sum of internal field sources, which includes the dipolar fields of nuclear and electronic moments, and the contact hyperfine field due to a net spin density of conduction electrons at the muon site. The functional form of the relaxation of the ZF-μSR signal is dependent on the arrangement and fluctuation rate of the internal field sources.

2.2.1 Magnetic Order

In the presence of magnetic order, muons stopping at the same site in the crystal lattice experience the same net dipolar field from the ordered electronic moments and consequently coherently precess. In this case the ZF-μSR spectrum is described by

$$P(t) = G(t)\cos(\gamma_{\mu}\left\langle B_{\mu}\right\rangle t)\,, \tag{2.7}$$

where $\left\langle B_{\mu}\right\rangle$ is the average local magnetic field at the muon site, and $G(t)$ is a relaxation function due to various factors, such as a finite magnetic correlation length, fluctuations and/or sources of random fields (*e.g.* nuclear dipole moments). Hence the signature of

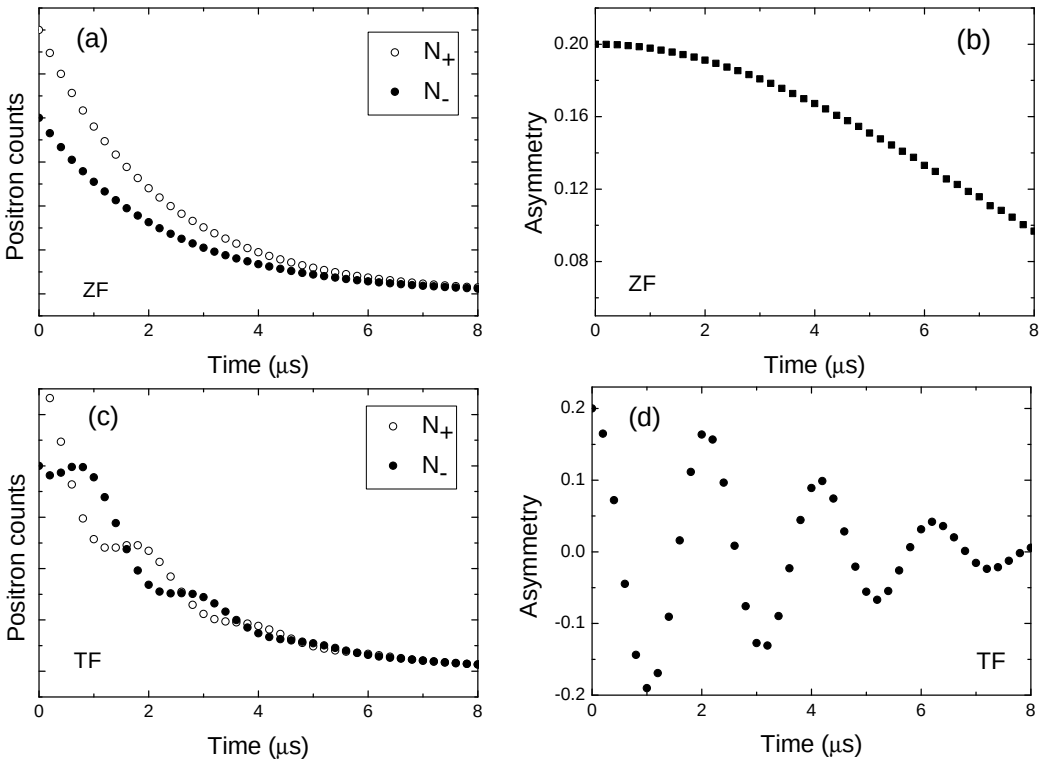

Figure 2.3: Theoretical simulations of the positron detector time histograms defined in Eq. (2.5) for a (a) ZF-μSR and, (c) TF-μSR configuration, (b) and (d) show the corresponding asymmetry spectrum $A(t)$. The ZF-μSR simulation assumes a single Gaussian damping of $P(t)$ with time, and the TF-μSR spectrum assumes that $P(t)$ is a Gaussian-damped cosine function with a frequency corresponding to the applied transverse magnetic field. Note $a_{\rm o} = 0.2$ is assumed for both simulations.

magnetic order in a ZF-μSR experiment is the observation of a coherent oscillation. Multiple frequencies are observed when there is more than one, but only a few different muon stopping sites. Unfortunately, a determination of the magnetic structure by ZF-μSR is only possible when the muon site(s) is (are) known. When magnetic order is present only in part of the sample, $P(t)$ consists of a term like Eq. (2.7) with a fractional amplitude that reflects the volume fraction of magnetic order.

2.2.2 Randomly Oriented Static Magnetic Fields

In a sample with a dense system of randomly oriented magnetic dipole moments that are static on the μSR time scale (a few muon mean lifetimes τ_μ), the internal magnetic field distribution is a Gaussian function

$$n(B_i) = \frac{\gamma_\mu}{\sqrt{2\pi}\Delta} \exp\left(-\frac{\gamma_\mu^2 B_i^2}{2\Delta^2}\right), \quad (i = x, y, z). \tag{2.8}$$

where Δ/γ_μ is the width of the internal field distribution, and B_i are the field components. In this case there is no coherent precession of muon spins, only a loss of polarization, which is described by a static Gaussian Kubo-Toyabe relaxation function [41, 68]

$$G_{\mathrm{KT}}(t) = \frac{1}{3} + \frac{2}{3}(1 - \Delta^2 t^2) \exp\left(-\frac{1}{2}\Delta^2 t^2\right). \tag{2.9}$$

Figure 2.4 shows the static Gaussian Kubo-Toyabe relaxation function for different values of Δ. $G_{\mathrm{KT}}(t)$ is partially characterized by a 1/3 recovery of the muon spin polarization after sufficiently long time and is nonzero for all t. Often the host nuclei of a sample are treated as a dense system of randomly oriented magnetic dipole moments that are static on the μSR time scale. However, some ZF-μSR measurements of samples with the dominant field contribution originating from the nuclear spins show asymmetry spectra that deviate substantially from $G_{\mathrm{KT}}(t)$. Part of this thesis is dedicated to sorting out the nuclear contribution to the muon spin depolarization in the high-T_c superconductor $La_{2-x}Sr_xCuO_4$, by considering the full quantum mechanical Hamiltonian describing the interaction between the muon, nuclei and the crystal electric field gradient. It will be demonstrated that randomly oriented host nuclear spins do not in general lead to a static Gaussian Kubo-Toyabe type relaxation.

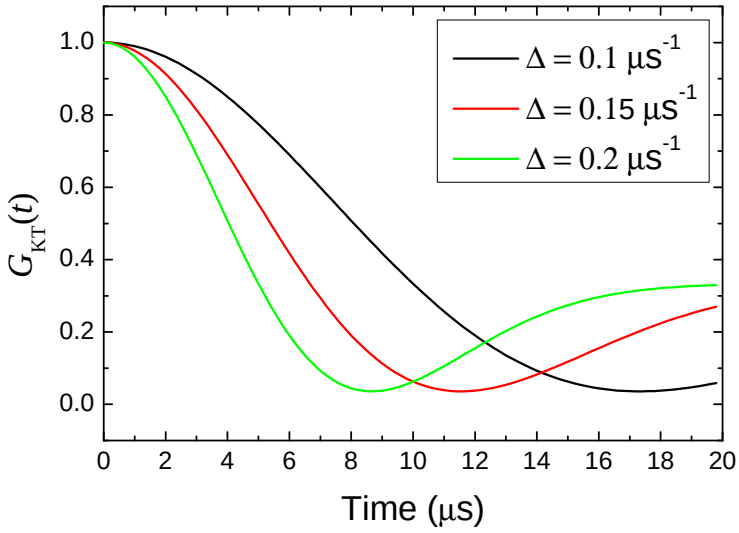

Figure 2.4: Static Gaussian Kubo-Toyabe muon spin relaxation function $G_{\mathrm{KT}}(t)$ for different values of Δ, where Δ/γ_μ is the width of the Gaussian internal field distribution.

In contrast to a dense system of magnetic dipole moments, a spatially dilute system of magnetic moments has an approximately Lorentzian distribution of field [69]

$$n(B_i) = \frac{\gamma_\mu}{\pi}\frac{a}{a^2+\gamma_\mu^2 B_i^2}, \quad (i = x,y,z), \tag{2.10}$$

where a/γ_μ is the half-width at half-maximum (HWHM) of the field distribution and B_i are the field components. For a Lorentzian distribution of internal fields, the static Kubo-Toyabe function is [70]

$$G_L(t) = \frac{1}{3} + \frac{2}{3}(1-at)\exp(-at). \tag{2.11}$$

Figure 2.5 shows how the Lorentzian Kubo-Toyabe function depends on a. This function is characterized by an exponential damping at early times, and a shallower minimum compared to the Gaussian function of Eq. (2.9).

2.2.3 Fluctuating Magnetic Fields

Fluctuations of the local magnetic field modify the muon spin relaxation, as in this case the muons sense time-varying fields. For the purpose of this thesis we restrict the discussion

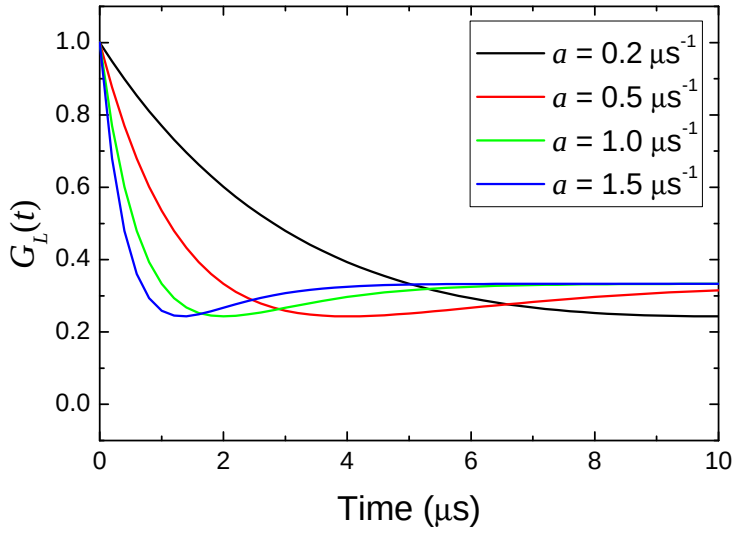

Figure 2.5: Static Lorentzian Kubo-Toyabe function $G_L(t)$ for different values of a, where a/γ_μ is the HWHM of the static Lorentzian internal field distribution.

of the effect of fluctuations on the ZF-μSR signal to the case of a Gaussian distribution of internal fields. In general, the dynamical relaxation function must be calculated numerically. However, for sufficiently fast fluctuations, the muon spin relaxation function is well approximated by the following analytical expression [71]

$$G(t) = \exp\left[-2(\Delta^2/\nu^2)\left(e^{-\nu t} - 1 + \nu t\right)\right], \tag{2.12}$$

where ν is the fluctuation rate of the internal field. In the fast fluctuation limit, (*i.e.* $\nu/\Delta \gg 1$), this approaches the following exponential relaxation function

$$G(t) = \exp(-2\Delta^2 t/\nu). \tag{2.13}$$

Figure 2.6 shows how the muon spin relaxation function for a Gaussian distribution of internal magnetic fields is modified by fluctuations. Faster fluctuations of the local internal magnetic field result in a slower relaxation of the ZF-μSR signal.

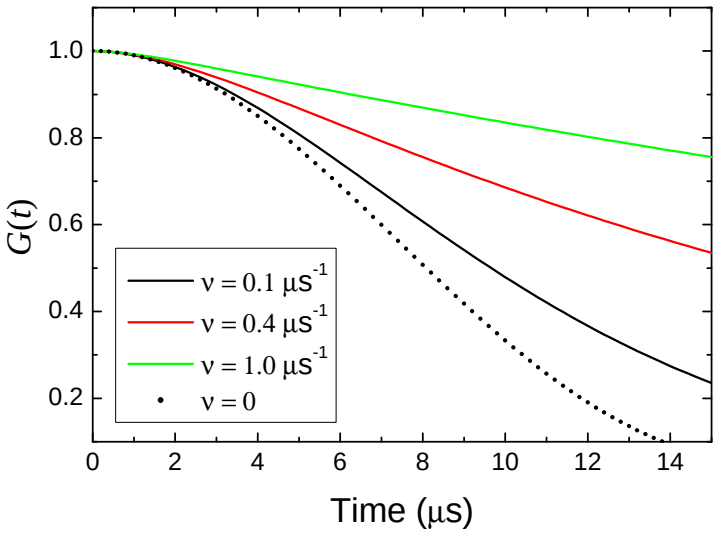

Figure 2.6: ZF-μSR relaxation function of Eq. (2.12) for a Gaussian distribution of fast fluctuating internal magnetic fields with different fluctuation rates ν. The width of the distribution of fields is Δ/γ_μ, with $\Delta = 0.1\ \mu s^{-1}$. Also shown is the corresponding static Gaussian Kubo-Toyabe function (dotted curve).

2.3 TF-μSR

Transverse-field (TF) μSR involves the application of an external magnetic field perpendicular (transverse) to the initial muon spin polarization $\mathbf{P}(0)$. It is widely used to measure the magnetic response of a material in the bulk. Particularly, as will be discussed in the next chapter, TF-μSR can be used to determine the internal magnetic field distribution of a type-II superconductor in the vortex state to obtain information on the superconducting pairing symmetry.

In a TF-μSR experiment the effective magnetic field acting on the muon spin is the vector sum of both external and internal field sources. Similar to the ZF-μSR case, the functional form of the relaxation of the TF-μSR signal is also solely dependent on the arrangement and fluctuation rate of the internal field sources, assuming a homogeneous static external magnetic field is applied.

2.3.1 Static Magnetic Fields

A dense system of randomly oriented magnetic dipole moments that are static on the μSR time scale creates a Gaussian distribution of internal fields, which results in a Gaussian damping of the muon spin polarization [66]

$$G_{\mathrm{TF}}(t) = \exp(-\sigma^2 t^2/2)\,, \tag{2.14}$$

where σ/γ_μ is the width of the Gaussian field distribution along the direction of the external field. The depolarization rate σ can depend on both the direction and the strength of the external field. In the latter case, σ can be reduced due to the rapid precession of the magnetic dipole moments about the external field. The effect of the host nuclei on the TF-μSR signal is often well approximated by this Gaussian depolarization function.

On the other hand, in a dilute system of magnetic dipole moments, the muon spin polarization is described by an exponential relaxation function corresponding to a Lorentzian distribution of internal fields

$$G_{\mathrm{TF}}(t) = \exp(-\Lambda t)\,. \tag{2.15}$$

2.3.2 Fluctuating Magnetic Fields

Similar to the ZF-μSR case, fluctuations modify the form of the TF-μSR depolarization function. In a fluctuating dense system of magnetic dipole moments, the muon spin depolarization is described by the so-called Abragam formula [72]

$$G_{\mathrm{TF}}(t) = \exp\left[-(\sigma^2/\nu^2)\left(e^{-\nu t} - 1 + \nu t\right)\right], \tag{2.16}$$

where ν is the fluctuation rate of the local field. This depolarization function differs from Eq. (2.12) by a factor of 2 in the exponential. This is due to the fact that in the ZF-μSR configuration, the muon spin is depolarized by two components of the internal field perpendicular to the initial muon spin polarization, while in the TF-μSR configuration, only the component along the direction of the external field contributes to the muon spin depolarization. In the limit of fast fluctuations, an exponential relaxation is obtained (*i.e.* $G_{\mathrm{TF}} = \exp(-\sigma^2 t/\nu) = \exp(-\Lambda t)$). Note that the exponential relaxation rate Λ becomes smaller as the fluctuation rate ν increases.

Chapter 3

TF-μSR in the Superconducting Vortex State

TF-μSR has been widely used for measurements in the vortex state of superconductors. This chapter discusses how TF-μSR is used to extract information on the magnetic penetration depth λ, and hence the superconducting pairing symmetry.

3.1 Magnetic Field Distribution $n(B)$ in the Vortex State

In the vortex state of a type-II superconductor, the internal magnetic field distribution $n(B)$ is spatially inhomogeneous (see inset of Fig. 3.1). An analytical expression for the spatial field variation of an ideal vortex lattice has been derived from the Ginzburg-Landau (GL) theory. In particular [52],

$$B(\mathbf{r}) = B_{\mathrm{o}}(1-b^4)\sum_{\mathbf{G}} \frac{e^{-i\mathbf{G}\cdot\mathbf{r}} u K_1(u)}{\lambda^2 G^2}\,, \tag{3.1}$$

where $b = B/B_{c2}$ and

$$u^2 = 2\xi^2 G^2 (1+b^4)[1-2b(1-b)^2]\,. \tag{3.2}$$

In Eq. (3.1), B_{o} is close to the applied field, $\mathbf{G}$ are the reciprocal lattice vectors of the periodic array of vortices, and $K_1(u)$ is a modified Bessel function. Within this model, the precise shape of the internal magnetic field distribution $n(B)$, with $n(B)dB$ being the probability of finding a magnetic field between B and $B+dB$, is determined by the geometric

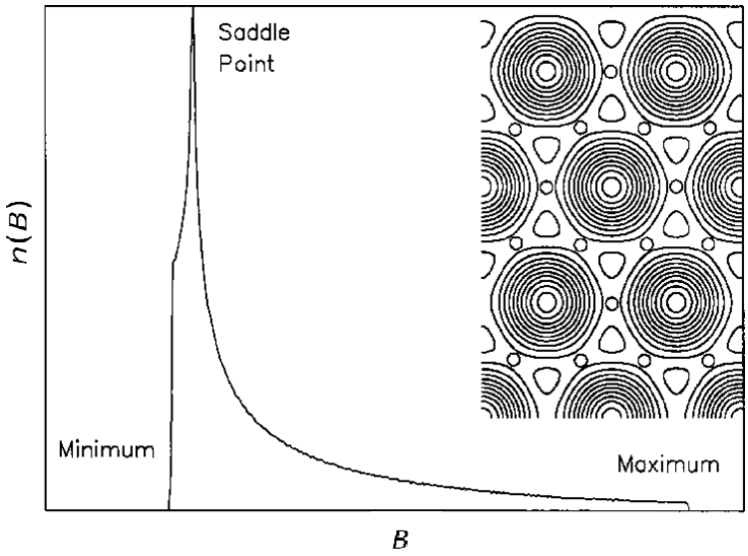

Figure 3.1: The internal magnetic field distribution $n(B)$ of an ideal hexagonal vortex lattice of a type-II superconductor. The inset is a contour plot of the corresponding spatial field profile $B(\mathbf{r})$.

arrangement of the vortex lattice, the magnetic penetration depth λ and the superconducting coherence length ξ.

Figure 3.1 shows $n(B)$ for an ideal hexagonal vortex lattice generated from Eq. (3.1). The sharp cutoff on the low-field side is the minimum internal field occurring at the centre of the triangle formed by three adjacent vortices. The sharp peak is the van Hove singularity produced by the saddle point field midway between nearest neighbour vortices. The long high-field tail originates from the distribution of field around the vortex cores, and the high-field cutoff is the maximum field at the centre of the vortex cores. From a measurement of $n(B)$ in the vortex state, one can in principle determine the fundamental length scales λ and ξ by analysis with Eq. (3.1). However, in a real superconductor, there can be strong deviations from the ideal vortex lattice, as described in the following.

3.2 TF-μSR Measurements of the Vortex State

Since the typical vortex lattice spacing in TF-μSR experiments with $H \ll H_{c2}$ is $\sim 10^2$ - 10^3 times larger than the dimensions of the crystallographic unit cell, the muon stops randomly on the length scale of the vortex lattice. Consequently, the implanted muons randomly sample the internal magnetic field distribution $n(B)$. In TF-μSR measurements of the vortex state of superconductors, the time evolution of the muon spin polarization is related to $n(B)$ as follows

$$P(t) = \int_0^\infty n(B) e^{i\gamma_\mu B t} dB \,. \tag{3.3}$$

Generally, the TF-μSR signal is fit in the time domain, although an inverse Fourier transform of $P(t)$ yields a visual approximation of the internal magnetic field distribution (often referred to as the TF-μSR "line shape")

$$n(B) = \int_0^\infty P(t) e^{-i\gamma_\mu B t} dt \,. \tag{3.4}$$

The Fourier transform is an approximation of $n(B)$ because of the muon life time. In particular, $P(t)$ has a finite time range ($\sim 10\,\mu$s) and an uncertainty that grows exponentially with increasing time.

The field distribution $n(B)$ can also be obtained from NMR experiments, although it is often broadened by the additional quadrupolar interaction if the nucleus carries a spin $I > 1/2$. In addition to being a pure magnetic probe, the TF-μSR technique has other advantages over NMR. For example, due to screening of the RF field in the superconducting state, conventional NMR is generally limited to polycrystalline samples or small single crystals, whereas μSR can be easily performed on single crystals of any size.

The dominant contribution to the TF-μSR signal in the vortex state of a superconductor is the inhomogeneous magnetic field distribution associated with the vortex lattice, which is parameterized by λ and ξ in the analytical GL model of Eq. (3.1). Fits of the TF-μSR signal that are sensitive to the high-field cutoff of $n(B)$, are sensitive to the size of the vortex cores [76]. However, the accuracy of these kinds of measurements depends on the uniformity of the vortex lattice in the sample. This is particularly limiting in measurements on unoriented polycrystalline samples, where, because $n(B)$ is nearly symmetric [74], the line broadening effects and disorder cannot be easily isolated. The task is less formidable

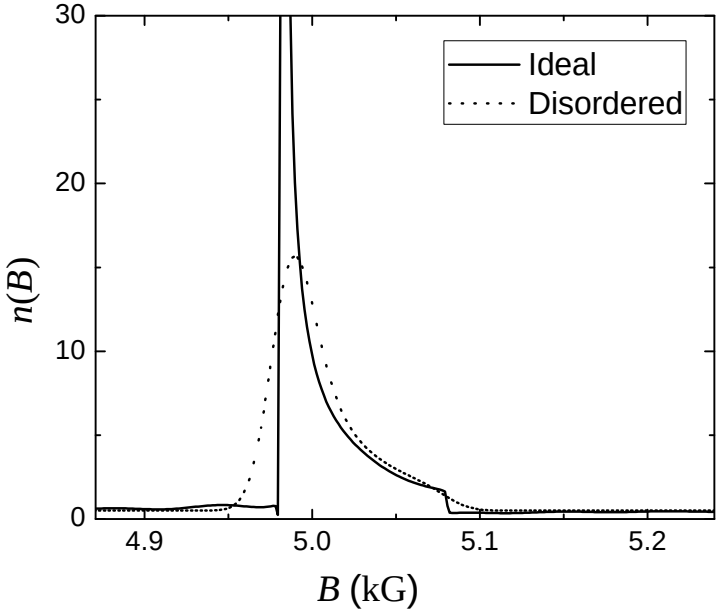

Figure 3.2: Fourier transforms of a theoretical muon spin polarization function $P(t)$ for an ideal hexagonal vortex lattice (solid curve) and for a disordered vortex lattice (dotted curve). In both cases a spatial field profile $B(\mathbf{r})$ given by Eq. (3.1) was assumed, with $\lambda = 1500$ Å, $\xi = 100$ Å and $B_o = 5$ kG. For the disordered lattice, $P(t)$ is multiplied by a Gaussian depolarization function $\exp(-\sigma^2 t^2/2)$ with $\sigma = 1\ \mu s^{-1}$ to simulate a 3.4% (relative to the nearest-neighbour intervortex spacing) RMS deviation of the vortices from their ideal positions.

for single crystals, where the contribution of the vortex lattice to $n(B)$ is highly asymmetric (see Fig. 3.1).

Line broadening caused by magnetic dipole moments (nuclear and/or electronic), and random frozen disorder of the vortex lattice smear the sharp features of $n(B)$ for the ideal lattice. In the time domain these broadening effects are often accounted for by multiplying Eq. (3.3) with a Gaussian depolarization function [52, 76]

$$P(t) = G_{\rm TF}(t) \int_0^\infty n(B) e^{i\gamma_\mu B t} dB\,, \tag{3.5}$$

where

$$G_{\mathrm{TF}}(t) = \exp\left(-\frac{\sigma^2 t^2}{2}\right) = \exp\left(-\frac{\sigma_{\mathrm{nuc}}^2 + \sigma_{\mathrm{dis}}^2}{2} t^2\right). \tag{3.6}$$

Here σ_{nuc} is the contribution to the relaxation rate from random nuclear dipoles [66] and σ_{dis} is the contribution from random frozen disorder of the vortex lattice [74]. Figure 3.2 shows how line broadening due to vortex-lattice disorder smears out the sharp features of $n(B)$ of an ideal vortex lattice. Because σ_{nuc} is in general temperature independent, it is easily determined by measurements above T_c. However, σ_{dis} is generally dependent on the strength of the applied magnetic field, temperature and the quality of the sample.

While Gaussian broadening of $n(B)$ is a reasonable approximation for the case of weak random frozen disorder of the vortex lattice, it is not expected to be valid when there is a high degree of disorder. In the case of a highly disordered vortex lattice, the sharp features of the ideal $n(B)$ are severely smeared out. As will be shown in the next chapter, such strong deviation from an ideal vortex lattice introduces significant uncertainty in the value of λ determined by TF-μSR. At this point it is worth mentioning that the line broadening caused by static or slowly fluctuating electronic moments (which are not accounted for in Eq. (3.6)) is usually so severe that measurements of λ in such samples by TF-μSR is usually not possible [77], as will be discussed in the next chapter.

Chapter 4

Effect of Vortex Lattice Disorder on TF-μSR Measurements of the Magnetic Penetration Depth

4.1 Introduction

In TF-μSR studies of type-II superconductors in the vortex state [52], a general assumption is that the vortex lattice is highly ordered. However, as mentioned earlier, this is not the case in many of the recently discovered doped iron-arsenic superconductors [59, 60, 61, 62, 63, 64, 65]. In addition to further line broadening, for single crystals such strong disorder smears out the high-field cutoff of the TF-μSR line shape. Here it is shown that although TF-μSR measurements of single crystal $BaFe_{2-x}Co_xAs_2$ exhibit asymmetric line shapes seemingly indicative of a well-ordered vortex lattice, fits to such data are insensitive to the high-field cutoff. In particular, there is an insensitivity to the fit parameter ξ in Eq. (3.1). In $BaFe_{2-x}Co_xAs_2$ this is partly due to electronic moments influenced by the applied magnetic field [77], but also strong disorder that appears to be generic to all doped iron-arsenic compounds. Since sensitivity of the fits to the high-field cutoff also influences the fitted value of the magnetic penetration depth λ [76], it is necessary to adequately account for the sources of smearing of the high-field tail.

Here TF-μSR measurements performed on an overdoped single crystal of $BaFe_{2-x}Co_xAs_2$

are presented. The effect of magnetism on the TF-μSR line shape and the complexity of accounting for the contribution from the electronic moments in the analysis is discussed. Next, details of a molecular dynamics (MD) method used to simulate the high degree of frozen disorder observed in the vortex lattice of overdoped $BaFe_{2-x}Co_xAs_2$ [63] are described. The resultant vortex configuration with the corresponding level of disorder is then used to calculate the magnetic field distribution $n(B)$, and subsequently compared to the standard method of convoluting $n(B)$ of the ideal lattice with a Gaussian distribution of fields.

4.2 Experiment

The TF-μSR experiments were performed on a $BaFe_{1.82}Co_{0.18}As_2$ ($T_c = 21$ K) single crystal provided by the Correlated Electron Materials Group at Oak Ridge National Laboratory. The sample was grown from a FeAs flux, as described elsewhere [82]. The crystal structure of the sample is shown in Fig. 4.1. Magnetic susceptibility measurements at 20 Oe show a sharp superconducting transition and complete diamagnetic screening, and energy dispersive x-ray spectroscopy measurements on different parts of the crystal indicate a uniform Co composition. High-statistics TF-μSR spectra of 20 million muon decay events were collected in magnetic fields $H = 0.02 - 0.5$ T applied transverse to the initial muon spin polarization $\mathbf{P}(0)$, and parallel to the crystallographic $\hat{c}$-axis (see Fig. 2.2).

The TF-μSR spectra were fitted in the time domain with Eq. (3.5), where the Gaussian depolarization function accounts for the effects of nuclear dipolar fields and random frozen vortex lattice disorder, and $n(B)$ is calculated from Eq. (3.1) for $T < T_c$. Figure 4.2 shows a set of representative TF-μSR time spectra in $BaFe_{1.82}Co_{0.18}As_2$ below and above T_c and the corresponding fits. The GL coherence length calculated from the upper critical field $H_{c2} \sim 50$ T of $BaFe_{1.84}Co_{0.16}As_2$ with $\mathbf{H} \parallel \hat{c}$ is $\xi_{ab} \sim \sqrt{\phi_o/\pi H_{c2}} \sim 26$ Å [84]. This represents a lower limit for the vortex core radius [76]. Yet fits of the TF-μSR spectra of $BaFe_{1.82}Co_{0.18}As_2$ show no sensitivity to the vortex cores at any field and converge with values of ξ approaching zero. Figure 4.3(a) shows that even at $H = 0.5$ T, where the vortex density is highest, a high-field cutoff is not discernible in the TF-μSR line shape. We next discuss one of the reasons for this.

Figure 4.4(a) shows the envelope of the TF-μSR signal at a temperature above T_c, and

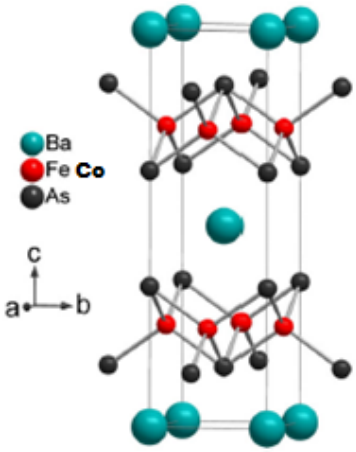

Figure 4.1: Schematic view of the crystal structure of $BaFe_{2-x}Co_xAs_2$, with a quasi-two-dimensional FeAs layer made of a square lattice of the Fe atoms in tetrahedrally coordinated bonds to As anions that are staggered below and above the Fe lattice.

at applied magnetic fields of 0.02 T and 0.5 T. The observed exponential depolarization is typical of dilute frozen spins or alternatively fast fluctuating electronic moments in a paramagnetic state (see Section. 2.3). The latter interpretation is consistent with the observation of a paramagnetic (PM) shift of the average internal field $\langle \mathbf{B}_\mu \rangle$ sensed by the muons at lower temperatures. This is evident in Fig. 4.4(b), which shows representative Fourier transforms of $P(t)$ at $H = 0.02$ T. Instead of the expected diamagnetic shift imposed by the superconducting state, $\langle \mathbf{B}_\mu \rangle$ exceeds H. The magnitude of the PM shift increases with increasing H and/or decreasing T.

The occurrence of a PM shift in the superconducting state of $BaFe_{2-x}Co_xAs_2$ and $SrFe_{2-x}Co_xAs_2$ has been reported by others [55, 58], and implies that the majority of the implanted muons sense an enhanced magnetic field due to the occurrence of magnetic order in a large volume of the sample. Magnetic order is known to exist in underdoped samples at $H = 0$ [79] and is apparently induced in overdoped samples by the applied field. It is well known that strong relaxation of the TF-μSR signal occurs even in long-range magnetically ordered systems, and with decreasing temperature there must be an increased broadening of $n(B)$ associated with the growth of the correlation time for spin fluctuations. Yet the effects of magnetism on the linewidth and functional form of $n(B)$ have not been previously

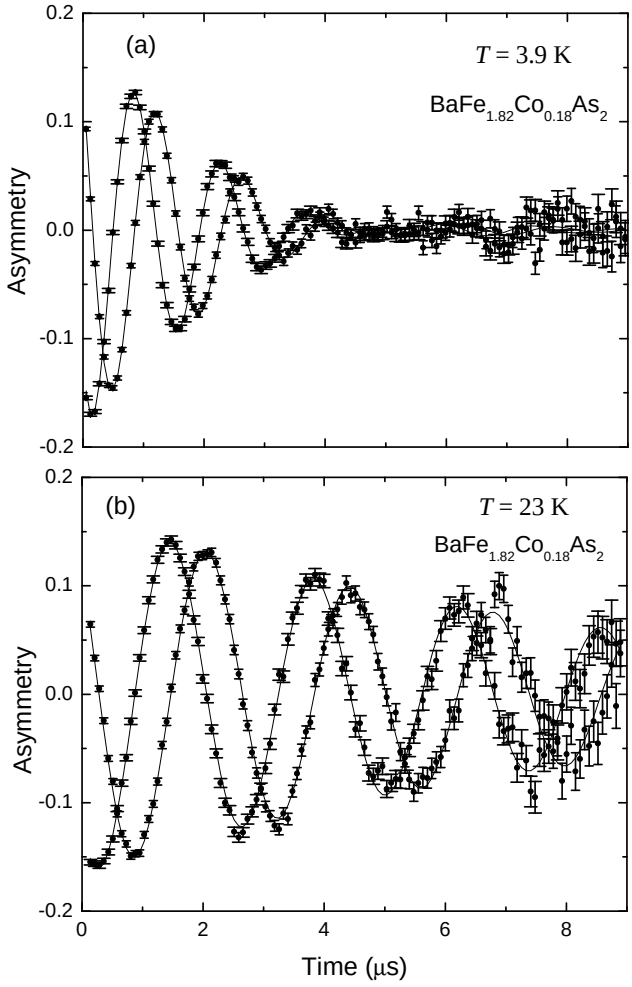

Figure 4.2: Real (from U and D positron detectors) and imaginary (from L and R positron detectors) part of the TF-μSR spectra of $BaFe_{1.82}Co_{0.18}As_2$ for an applied magnetic field $H = 0.5$ T, at (a) $T = 3.9$ K and (b) $T = 23$ K, respectively. The solid curves through the data points are fits of the TF-μSR spectra. The spectra in (a) are fitted to Eq. (3.5), yielding $\lambda = 2214$ Å, $\xi = 5$ Å, $\sigma = 0.251$ μs^{-1}, and a paramagnetic shift of 8.6 G which is discussed in the main text. In (b), the spectra are fitted to a depolarization function that is a product of exponential ($\exp(-\Lambda t)$) and Gaussian ($\exp(-\sigma^2 t^2/2)$) functions, yielding $\Lambda = 0.115 \pm 0.022$ μs^{-1} and $\sigma = 0$. Note that the spectra are plotted in a rotating reference frame (RRF), with an RRF frequency of 67.2 MHz.

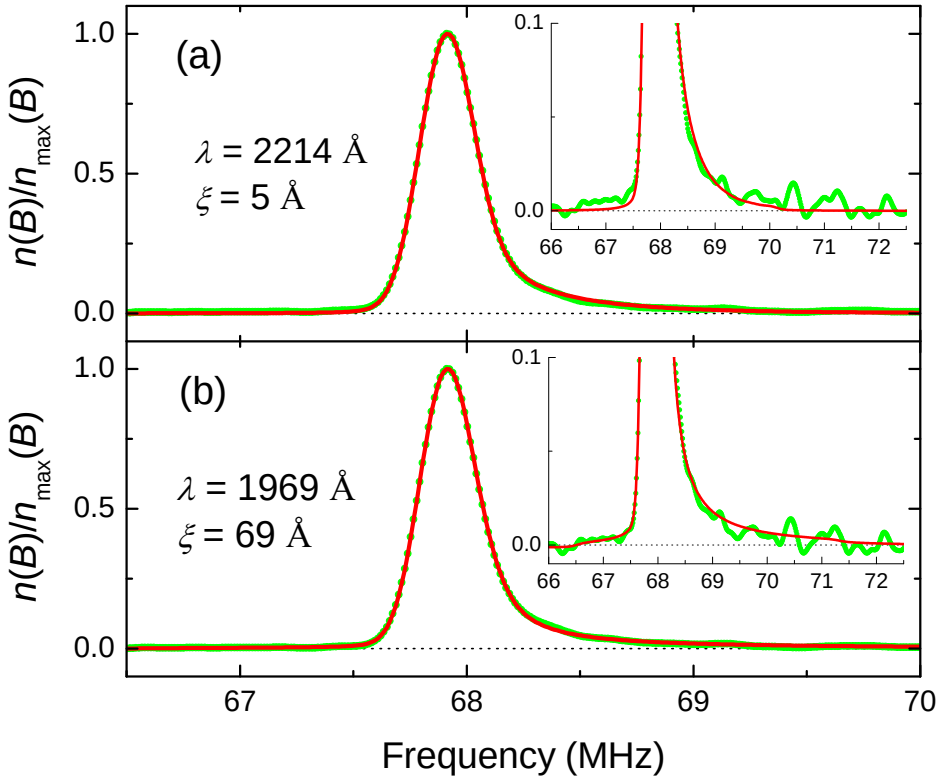

Figure 4.3: TF-μSR line shape of $BaFe_{1.82}Co_{0.18}As_2$ at $H = 0.5$ T and $T = 3.9$ K (green circles). (a) The red curve is the Fourier transform of the fit in the time domain which is presented in Fig. 4.2(a). (b) Fourier transform of a fit that assumes the model of field-induced AFM order described by Eq. (4.1) (red curve). The fit yields $\sigma = 0.251$ μs^{-1} and a PM shift of 8.6 G. Other fit parameters are shown in Fig. 4.5. Note the Fourier transforms have been normalized to their peak value $n_{\max}(B)$, and a Gaussian apodization has been used to smooth out some of the ringing caused by the finite time range and scatter of the data points at late times.

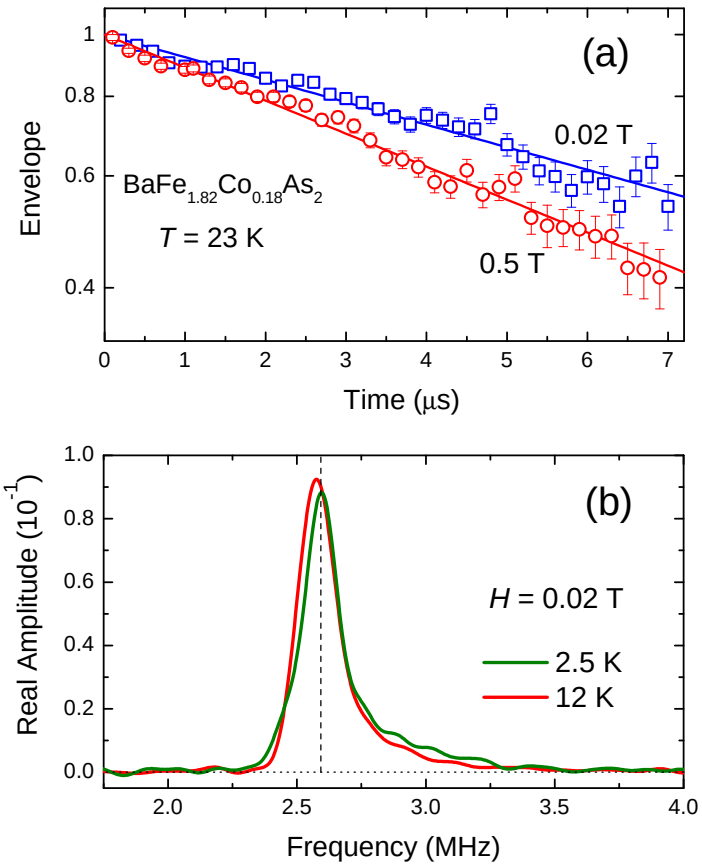

Figure 4.4: (a) Envelopes of TF-μSR spectra of $BaFe_{1.82}Co_{0.18}As_2$ in the normal state at $T = 23$ K. The solid curves are fits to a single exponential relaxation function $G(t) = \exp(-\Lambda t)$, yielding $\Lambda = 0.081 \pm 0.003$ μs^{-1} and $\Lambda = 0.119 \pm 0.003$ μs^{-1} at $H = 0.02$ T and $H = 0.5$ T, respectively. (b) TF-μSR line shapes of $BaFe_{1.82}Co_{0.18}As_2$ below T_c at $H = 0.02$ T. The dashed vertical line indicates the Larmor precession frequency of the muon in vacuum at the applied field H.

considered in TF-μSR studies of these compounds.

Accounting for such magnetism in the vortex state of $BaFe_{1.82}Co_{0.18}As_2$ is nontrivial because of the spatially varying superconducting order parameter and the likelihood that the field-induced magnetism occurs in a nematic phase [80]. Even so we have achieved excellent fits of the TF-μSR spectra of $BaFe_{1.82}Co_{0.18}As_2$ to polarization functions that incorporate different forms of enhanced magnetism in the vortex core region (*e.g.* commensurate spin-density wave, ferromagnetism, spin glass). We expect the magnetism to be strongest in the vortex core region where superconductivity is suppressed. As an example, typical results for fits to one of these models of magnetism in the vortex state is described next.

The model of magnetism considered here assumes the electronic moments on the Fe atoms are frozen and antiferromagnetically aligned in the vortex cores, but rapidly fluctuate in the spatial regions in between. Consequently, in addition to the usual practice of multiplying $P(t)$ by the Gaussian depolarization function of Eq. (3.6), $P(t)$ is multiplied by an exponential depolarization function $\exp(-\Lambda t)$, as observed above T_c, to account for the rapidly fluctuating magnetism outside the vortex cores. In addition, the AFM order in the vortex cores is modeled by adding the following term to Eq. (3.1)

$$B_{\rm AFM}(\mathbf{r}) = B_{\rm AFM} e^{-r^2/2\xi_{\rm AFM}^2} \sum_{\mathbf{K}} \left(e^{-i\mathbf{K}\cdot\mathbf{r}} - e^{-i\mathbf{K}\cdot\mathbf{r}'} \right) , \tag{4.1}$$

where $\mathbf{K}$ is the reciprocal lattice vector of the AFM square Fe sublattice of spacing 2.8 Å, $B_{\rm AFM}$ is the field amplitude, $\xi_{\rm AFM}$ governs a Gaussian radial decay of $B_{\rm AFM}$ from the core centre, and $\mathbf{r}$ and $\mathbf{r}'$ are the position vectors for "up" and "down" spins, respectively. Such localized magnetic order in the vortex core regions has the effect of smearing the high-field cutoff, but can also introduce a low-field tail in $n(B)$ [81]. As indicated by the large value of ξ in Fig. 4.3(b), fits to this model are sensitive to the vortex cores. Figure 4.5 shows the temperature dependence of the fitting parameters. As can be seen in Fig. 4.5(b), with decreasing temperature, the magnetism-induced depolarization evolves from exponential (Λ) to Gaussian (σ). Considering Eqs. (2.14) and (2.16), this indicates that at high temperatures (above T_c) the field-induced magnetism appears in the form of fast fluctuating electronic moments that slow down and eventually lead to a pure Gaussian depolarization at the lowest temperature. In addition, Figure 4.5(c) shows that both $B_{\rm AFM}$ and the ratio $\xi_{\rm AFM}/\xi$ increase with decreasing temperature, indicating that the magnetic order in the vortex cores

is enhanced and has a greater spatial extent about the vortex cores at lower temperatures.

Consistent with behaviour deduced from TF-μSR measurements on $BaFe_{1.772}Co_{0.228}As_2$ [57], fits to a model without magnetism that are insensitive to the vortex cores yield an unusual linear temperature dependence of $1/\lambda^2$ immediately below T_c and a saturation of λ at low T (see Fig. 4.5(a)). To achieve such fits it is necessary to fix ξ to a finite value. In this case ξ was fixed to be 5 Å at all temperatures. In contrast, fits assuming static AFM order in the vortex cores exhibit a linear temperature dependence well below T_c that is suggestive of nodes in the superconducting gap. However, these results simply demonstrate the ambiguity in modeling such data. Without knowledge of the precise form of the magnetism, the model presented here cannot be deemed rigorously valid. Next the effect of vortex lattice disorder on the TF-μSR line shapes of $BaFe_{1.82}Co_{0.18}As_2$ is considered.

4.3 Effect of Random Frozen Vortex Lattice Disorder

In this section the effects of random frozen vortex lattice disorder on the TF-μSR line shape is treated by numerical calculation. This rigorous approach is necessary due to the high degree of disorder observed in doped iron-arsenic superconductors, which cannot be accurately accounted for by simple Gaussian broadening (see Eq. (3.6)).

4.3.1 Simulation of a Disordered Vortex Lattice

To simulate vortex lattices bearing the degree of random frozen disorder observed in imaging and diffraction experiments on $BaFe_{2-x}Co_xAs_2$ at external fields $H \leq 0.5$ T, a molecular dynamics (MD) method is used that is based on the procedure developed in Ref. [83]. In the framework of Ginzburg-Landau (GL) theory, the interaction energy per unit length along the vortex line between vortices at positions $\mathbf{r}_i$ and $\mathbf{r}_j$ in a two-dimensional (2D) plane is [1]

$$\varepsilon(r_{ij}) = \frac{\Phi_o^2}{8\pi^2\lambda^2} K_0\left(\frac{r_{ij}}{\lambda}\right), \tag{4.2}$$

where r_{ij} is the separation between the vortices and K_0 is a zeroth-order Hankel function of imaginary argument [1]. The vortices in $BaFe_{1.82}Co_{0.18}As_2$ are arranged in a disordered hexagonal lattice. The intervortex spacing of an ideal hexagonal lattice is $a = \sqrt{2\phi_o/\sqrt{3}B}$.

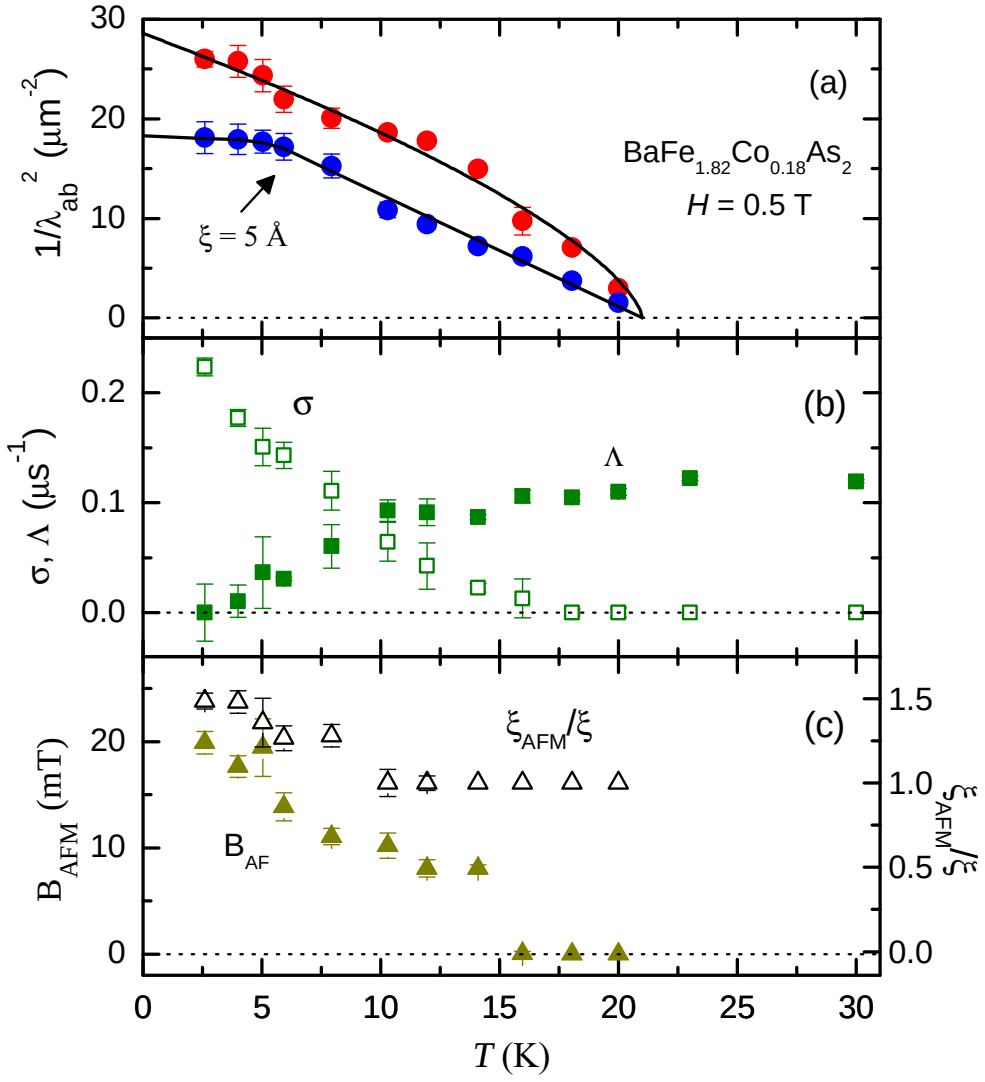

Figure 4.5: Results of fits of the TF-μSR time spectra of $BaFe_{1.82}Co_{0.18}As_2$ at $H = 0.5$ T, assuming the model of field-induced magnetic order described in the main text. Temperature dependence of (a) $1/\lambda^2$, (b) the depolarization rates σ (Gaussian) and Λ (exponential), (c) B_{AFM} and the ratio ξ_{AFM}/ξ. Also shown in (a) are results of fits without magnetic order, but with ξ fixed to be 5 Å (blue circles), as is necessary to achieve convergence.

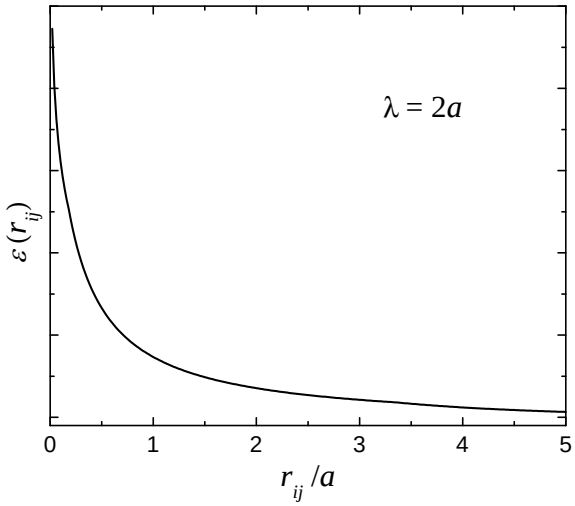

Figure 4.6: Plot of the intervortex interaction energy as a function of the separation r_{ij} between two vortices. Here the magnetic penetration depth $\lambda = 2a$, where a is the intervortex spacing in the ideal ordered lattice.

Hence at $H = 0.5$ T the average intervortex spacing is ~ 690 Å. On the other hand, the GL coherence length ξ estimated from the upper critical field H_{c2} of $BaFe_{1.84}Co_{0.16}As_2$ is ~ 26 Å [84]. Since the vortex core radius is approximately ξ, the core region accounts for $\sim 1\%$ of the sample volume. In this case the Hankel function $K_0(r_{ij}/\lambda)$ in Eq. (4.2) can be simply approximated by the two limiting forms $\sqrt{\pi\lambda/2r}\exp(-r/\lambda)$ at $r \to \infty$, and $\ln(\lambda/r) + 0.12$ for $\xi \ll r \ll \lambda$. Figure 4.6 shows the interaction energy as a function of the separation between two vortices.

In the simulation each vortex is considered as a point particle, with its position being the centre of the vortex core. Initially, a number of N vortices are sitting randomly within a circular region of radius $R \gg \lambda$, with a vortex density equivalent to that of the corresponding ideal hexagonal vortex lattice. In each MD step, the i^{th} vortex at position $\mathbf{r}_i(t)$ has an average velocity $\mathbf{v}_i(t)$ that is related to the force $\mathbf{F}(\mathbf{r}_i(t), t)$ acting on it as follows

$$\mathbf{v}_i(t) = \mathbf{F}(\mathbf{r}_i(t), t)/\eta\,, \tag{4.3}$$

where η is a frictional coefficient assumed be equal for all vortices, with $\eta = 1$ here. The

force $\mathbf{F}(\mathbf{r}_i(t),t)$ is given by

$$\mathbf{F}(\mathbf{r}_i(t),t) = -\nabla U(\mathbf{r}_i(t),t) + \mathbf{F}_{\text{cen}}(\mathbf{r}_i(t)) + \mathbf{F}_{\text{rand}}(t)\,. \tag{4.4}$$

Here U is the potential energy due to interactions with all other vortices at positions $r < R$. The force $\mathbf{F}_{\text{cen}}$ accounts for the interaction with an analogous distribution of vortices beyond $r = R$, and is evaluated numerically at each $r \leq R$ at the beginning of the simulation. The following approximation was used to ensure a uniform distribution of vortices for $r < R$

$$\mathbf{F}_{\text{cen}}(\mathbf{r}) = -\left(0.01 + 0.01\frac{r}{a}\right)\hat{r}\,, \quad (r \leq R) \tag{4.5}$$

The third term $\mathbf{F}_{\text{rand}}$ in Eq. (4.4) is a random force used to control the degree of disorder. At each MD step, the direction and magnitude of $\mathbf{F}_{\text{rand}}$ are random, with magnitude of F_{rand} being sampled from a symmetric probability distribution centred about $F_{\text{rand}} = 0$. The degree of disorder can be controlled by the magnitude of the standard deviation of $\mathbf{F}_{\text{rand}}$, which is denoted here as δF_{rand}.

In the MD method a modified "leapfrog" algorithm is used [83]

$$\mathbf{r}_i(t) = \mathbf{r}_i(t-\Delta t) + \frac{1}{2}[\mathbf{v}_i(t-\Delta t) + \mathbf{v}_i(t-2\Delta t)]\Delta t\,, \tag{4.6}$$

where $\mathbf{v}_i(t)$ is obtained from Eq. (4.3). To ensure faster stabilization of the vortex lattice, the time increments Δt were adjusted during the progression of the simulation so that at late times Δt is shorter. In our simulations, N_1 steps were taken with $\Delta t = \Delta t_1$, followed by N_2 steps with $\Delta t = \Delta t_2$, where $t_2 < t_1$ and $N_2 \geq N_1$. Because solid boundary conditions are implemented (*i.e.* the vortices are confined to $r \leq R$), after a sufficient number of MD steps the spatial region close to $r = R$ is more densely populated with vortices. To circumvent this problem, a narrow annular region near $r = R$ is removed prior to generating $n(B)$. As shown in Figs. 4.7(a) and 4.7(b), there is a uniform density of vortices in the remaining inner region.

Next, the separation $r_{ij} = \left|\mathbf{r}_i - \mathbf{r}_j\right|$ is calculated for a sufficiently large number of randomly chosen pairs of vortices in the resultant disordered lattice. The distribution of r_{ij} is an approximation of the so-called "radial distribution function" (RDF) [85], which reflects the degree of random frozen disorder of the vortex lattice. Figure 4.7(c) shows the RDF for the two simulated disordered lattices, together with that for an ideal lattice. The RDF of an

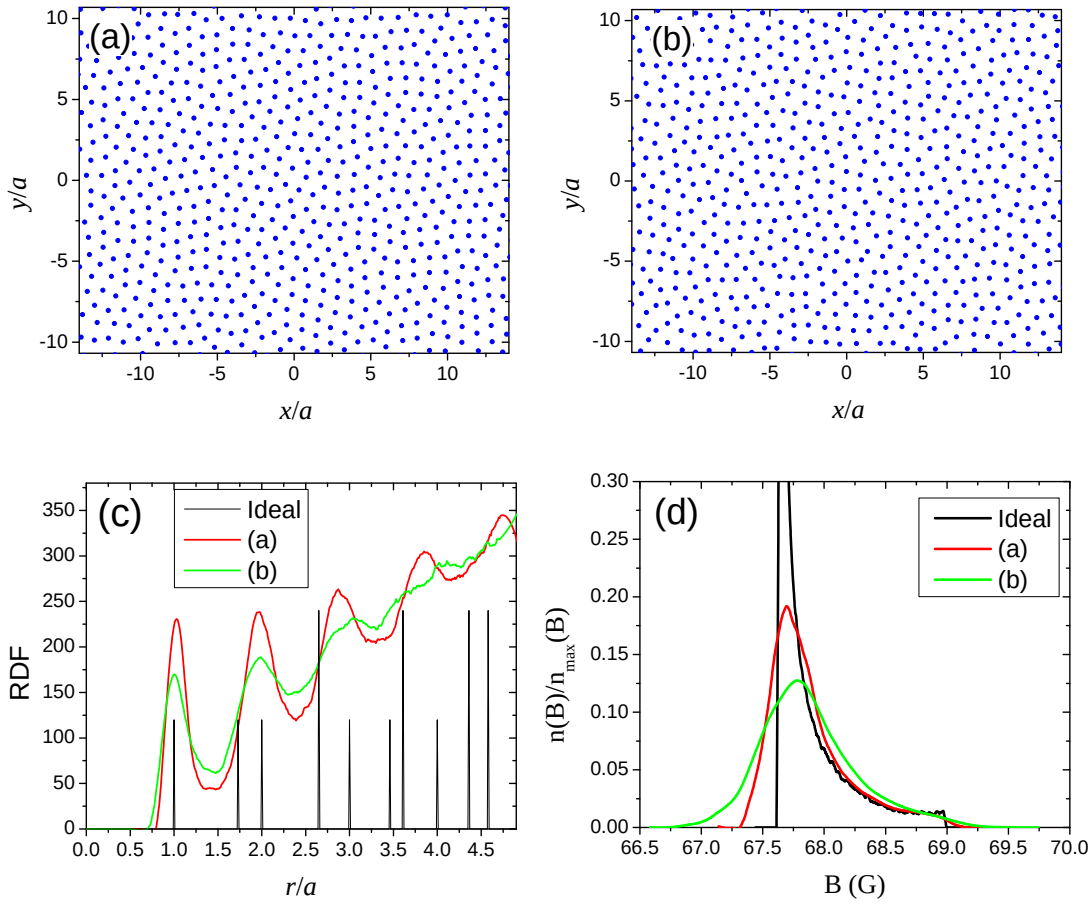

Figure 4.7: (a), (b) Simulated vortex lattices for two different degrees of random frozen disorder, generated after $N_1 = 500$ MD steps with time increment $\Delta t_1 = 0.002$ followed by $N_2 = 500$ MD steps with time increment $\Delta t_2 = 0.001$, with (a) $\delta F_{\text{rand}} = 0.2$ and (b) $\delta F_{\text{rand}} = 1.5$. A total number of $N = 5000$ vortices were used in both simulations. The horizontal and vertical scales are normalized with respect to the intervortex spacing of the ideal vortex lattice. (c) RDF of the ideal lattice and the disordered lattices of (a) (red) and (b) (green). (d) $n(B)$ of the ideal hexagonal vortex lattice (black), and vortex lattices of (a) (red) and (b) (green). Note $n(B)$ is normalized with respect to the peak height of the field distribution of the ideal vortex lattice $n_{\text{max}}(B)$. In all three simulations, the density of vortices and the magnetic field profile of the individual vortices are the same.

ideal vortex lattice is a sum of delta functions. However, the RDF for the simulated disordered vortex lattice is characterized by peaks centered at different values of r. The widths of these peaks increase with increasing r and increasing degree of disorder (see Fig. 4.7(c)).

4.3.2 Magnetic Field Distribution

The form of the magnetic field profile $B(r)$ of an individual vortex in the simulations (see Fig. 1.2) was chosen such that $n(B)$ of a perfectly ordered hexagonal vortex lattice resembles that generated by the analytical GL model [86]. To determine $n(B)$ of the simulated disordered vortex lattice, a small region about $r = 0$ was chosen for sampling. The local field B at randomly chosen sites in this region was calculated by summing up the individual field profiles of all vortices. The $n(B)$ corresponding to the vortex arrangements in Figs. 4.7(a) and (b), along with that for a perfectly ordered hexagonal lattice, are shown in Fig. 4.7(d). As expected, line broadening and smearing of the high-field cutoff is enhanced with an increasing degree of random frozen disorder.

Figure 4.8(a) shows two different magnetic field distributions of an ideal hexagonal vortex lattice generated from the analytical GL model. In Fig. 4.8(b) we show these same field distributions convoluted by a broad Gaussian distribution of field, and compared to a MD simulation characterized by an RDF resembling that determined experimentally for $BaFe_{1.81}Co_{0.19}As_2$ [63] (see Fig. 4.9). Note the difference between both the horizontal and vertical scales for Figs. 4.8(a) and 4.8(b). The standard approach of modeling vortex-lattice disorder in TF-μSR studies of single crystals fails to precisely describe the field distribution produced by the MD method. Furthermore, because the degree of disorder is substantial, the large Gaussian broadening means that the fitting parameters λ and ξ are no longer unique. This is demonstrated in Fig. 4.8(b), where very similar line shapes are obtained for very different values of λ and ξ.

It has been shown here that field-induced magnetism and/or random frozen disorder introduce considerable uncertainty in the values of λ deduced from TF-μSR measurements. Note that disorder in the sample also limits the mean free path of the charge carriers and causes pair breaking that affects λ. It is a major challenge to model these contributions to $n(B)$ in a reliable way. An additional complication to the problem is that precise knowledge of how these two factors evolve with temperature is lacking. Consequently, caution is

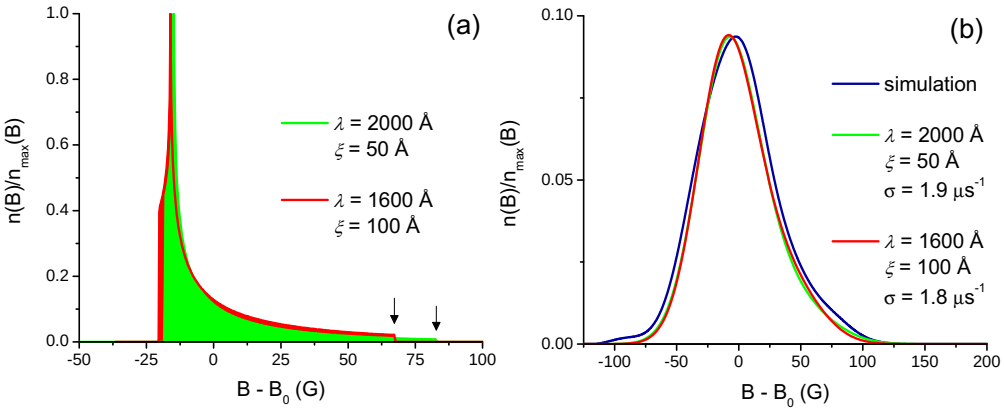

Figure 4.8: (a) Magnetic field distribution of an ideal hexagonal vortex lattice generated from an analytical GL model [86] for two different sets of the parameters λ and ξ. (b) Magnetic field distribution of a simulated highly disordered lattice with a RDF closely resembling that of $BaFe_{1.81}Co_{0.19}As_2$ [77] (see Fig. 4.9). Also shown are the field distributions of (a) convoluted with a Gaussian distribution of fields corresponding to a Gaussian relaxation rate σ in the time domain.

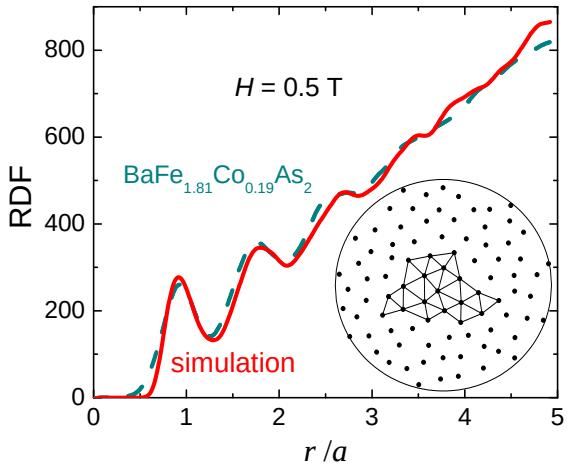

Figure 4.9: Radial distribution function (RDF) of the vortex lattice of $BaFe_{1.81}Co_{0.19}As_2$ at $H = 0.5$ T from Ref [63] (dashed curve) and of the simulated disordered vortex lattice shown in the lower right generated by molecular dynamics (MD). The horizontal scale is normalized with respect to the intervortex spacing $a = 691$ Å of the ideal hexagonal vortex lattice.

warranted in drawing conclusions about the symmetry of the superconducting pairing gap from TF-μSR measurements on doped iron-arsenic superconductors.

Chapter 5

Nuclear Contribution to the ZF-μSR Spectrum

5.1 Introduction

Recently, zero-field (ZF) μSR has been used to search for weak magnetism associated with possible loop-current order in the pseudogap region [40] and ferromagnetism in the heavily overdoped regime [88] of single crystal $La_{2-x}Sr_xCuO_4$ (LSCO). A nuisance in these measurements is the contribution of the nuclear dipoles, which can be the dominant relaxation mechanism. The contribution of the nuclear dipoles to the single crystal ZF-μSR signal is not only dependent on the muon site, but also on the orientation of the initial muon spin polarization $\mathbf{P}(0)$ with respect to the crystallographic axes. When $\mathbf{P}(0)$ is parallel to the $\hat{c}$-axis, the ZF-μSR spectrum of single crystal LSCO over a wide doping range is approximately described by a static Gaussian Kubo-Toyabe function $G_{\rm KT}(t)$ (see Eq. (2.9)). However, this is not the case when $\mathbf{P}(0)$ is perpendicular to the $\hat{c}$-axis. In particular, $P(t)$ deviates substantially from $G_{\rm KT}(t)$ beyond $t \sim 6$ μs and dips below zero at $t \sim 8$ μs [40]. Consequently, fitting with Eq. (2.9) requires truncating the ZF-μSR signal.

Here two advances in the application of ZF-μSR to studies of LSCO single crystals are presented. First, ZF-μSR spectra consisting of a high enough number of counts are presented to deduce whether static magnetic order exists. Secondly, an attempt is made to model more accurately the contribution of the host nuclei to the ZF-μSR signal of sin-

gle crystal LSCO, and to determine possible muon stopping sites via a comparison of the calculations to the measured ZF-μSR spectra.

5.2 Experiment

The experiments were performed on platelet-like single crystals of $La_{2-x}Sr_xCuO_4$ (LSCO) provided by Seiki Komiya and his research group from Central Research Institute of Electric Power Industry, Tokyo, Japan. The samples were cut from a traveling-solvent floating zone (TSFZ) growth rod. The TSFZ growth procedure that was followed is described in Ref. [89]. The single crystals cut from the TSFZ rod were annealed at 800 °C to 900 °C in an oxygen partial pressure to remove oxygen defects in accordance with the oxygen nonstoichiometry of LSCO [90]. Magnetic susceptibility measurements of the bulk superconducting transition temperature by a superconducting quantum interference device (SQUID) yielded $T_c = 37.6,\ 37.3,\ 30$, and 17 K for $x = 0.15$, 0.166, 0.216, and 0.24 samples, respectively. Note that the Sr content x is equivalent to the hole doping concentration. Figure. 5.1 shows the pseudogap temperature T^* from Ref. [94] and the superconducting transition temperatures for the samples studied here. ling-solvent floating zone (TSFZ) growth rod. The TSFZ growth procedure that was followed is described in Ref. [89]. The single crystals cut from the TSFZ rod were annealed at 800 °C to 900 °C in an oxygen partial pressure to remove oxygen defects in accordance with the oxygen nonstoichiometry of LSCO [90]. Magnetic susceptibility measurements of the bulk superconducting transition temperature by a superconducting quantum interference device (SQUID) yielded $T_c = 37.6,\ 37.3,\ 30$, and 17 K for $x = 0.15$, 0.166, 0.216, and 0.24 samples, respectively. Note that the Sr content x is equivalent to the hole doping concentration. Figure. 5.1 shows the pseudogap temperature T^* from Ref. [94] and the superconducting transition temperatures for the samples studied here.

ZF-μSR measurements of the LSCO single crystals were performed on the M15 and M20B surface muon beam lines at TRIUMF. The samples were mounted with the crystallographic $\hat{c}$-axis parallel to the muon beam momentum (see Fig. 2.2). The initial muon spin polarization $\mathbf{P}(0)$ was oriented perpendicular to the $\hat{c}$-axis of the LSCO single crystals using a Wien filter. This has the advantage that neither positron detector directly faces the incoming muon beam, which has a certain degree of positron contamination. The recorded

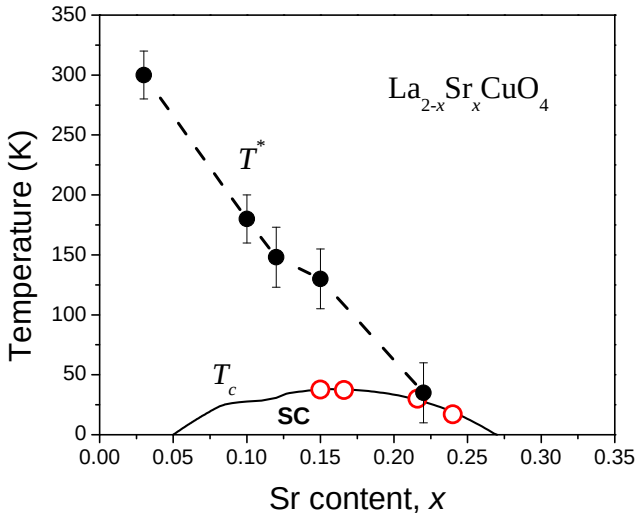

Figure 5.1: The pseudogap temperature T^* (solid circles) adapted from Ref. [94] and the superconducting transition temperature T_c (open circles) for the LSCO samples studied here.

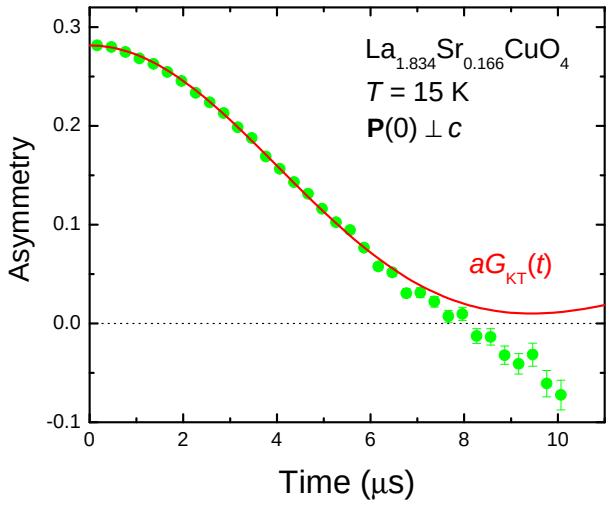

Figure 5.2: ZF-μSR signal of a $x = 0.166$ LSCO single crystal at $T = 15$ K recorded with the initial muon spin polarization $\mathbf{P}(0)$ perpendicular to the $\hat{c}$-axis. The solid curve is a fit of the data below $t = 6$ μs to Eq. (2.9).

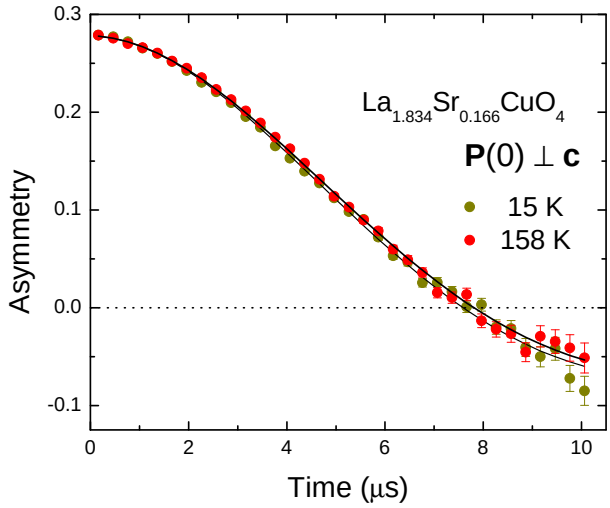

Figure 5.3: Comparison of the ZF-μSR signals of the $x = 0.166$ LSCO at $T = 15$ K and $T = 158$ K measured over a 10 μs time range. The solid curves are fits to the relaxation function Eq. (5.1).

spectra contain ~ 12 million muon decay events, sufficient to determine the late time ZF-μSR signal at $t > 8$ μs.

For all of the samples studied here, the static Gaussian Kubo-Toyabe function $G_{\rm KT}(t)$ fails to describe the ZF-μSR spectra when $\mathbf{P}(0) \perp \hat{c}$. Figure 5.2 shows the ZF-μSR signal for the $x = 0.166$ sample, which starts to deviate from $G_{\rm KT}(t)$ at $t \sim 6$ μs. To more accurately describe variations in the functional form of the ZF-μSR signal as a function of temperature and hole doping x, we fit the ZF-μSR spectra to a simple phenomenological relaxation function

$$G(t) = \exp[-(\Lambda t)^K] \cos[\nu(T) t], \tag{5.1}$$

with the relaxation rate Λ and the exponent K treated as temperature independent quantities, and the frequency ν being the only fitting parameter allowed to vary with temperature. Figure 5.3 shows representative ZF-μSR spectra for the $x = 0.166$ sample that are well described by Eq. (5.1) over the entire 10 μs time range. The evolution of the ZF-μSR signal with temperature is reflected in the temperature dependence of ν shown in Fig. 5.4(a). Note that $T > 150$ K is above the pseudogap temperatures T^* of the $x = 0.166$, 0.216 and

0.24 samples, as can be seen in Fig. 5.1. Consistent with the findings of MacDougall *et al.* [40], the ZF-μSR signal does not exhibit a temperature dependence characteristic of a magnetic phase transition in any of the samples studied. At $T = 200$ K, the value of ν is clearly reduced, but by the same amount for the $x = 0.15$ and $x = 0.24$ samples (see Fig. 5.4(a)). Hence the reduction of ν at high temperatures is attributed to muon diffusion, whereby the mobile μ^+ sees a time-averaged field over its life time. This same conclusion was reached in Ref. [40]. The weak temperature dependences of Λ and K below $x \sim 0.22$ likely reflects the effects of the Sr substitution, which slightly modifies the nuclear dipole contribution to the relaxation, but it may also reflect possible effects of having the initial muon spin polarization $\mathbf{P}(0)$ oriented in a different direction in the *ab* plane (see Sec. 5.7). The distinct drop in these parameters for the $x = 0.24$ sample may be associated with electronic phase separation into hole-rich and hole-poor regions. Evidence for electronic phase separation in overdoped LSCO is reported elsewhere (see for example Ref. [91]). This distinct drop may also be related to an anomalous occurrence of Curie paramagnetism in overdoped LSCO [92, 93, 95]. These fluctuating paramagnetic moments may lead to a more exponential muon spin relaxation (see Sec. 2.2.3), corresponding to smaller Λ and K values.

Weak magnetic order resembling that in the theoretical CC phase was observed in polarized neutron scattering measurements of YBCO single crystals [21, 22, 23]. However, a ZF-μSR study [36] of the same $YBa_2Cu_3O_{6.6}$ single crystal examined in the neutron scattering experiment of Ref. [22] shows that the weak magnetic order is discernible as a small-amplitude, rapidly damped oscillatory component in the early time range of the ZF-μSR signal. This indicates that the magnetic order occupies only a small volume fraction of the sample ($\sim$ 3%), and hence is a minority phase. The early time range of the ZF-μSR signal of the $x = 0.166$ LSCO sample is shown in Fig. 5.5. There is no evidence of a small-amplitude oscillatory component. Examination of the early time ZF-μSR spectra of the other LSCO samples likewise does not reveal evidence for the unusual weak magnetic order observed by polarized neutron scattering, which in LSCO is short range [23].

It is fairly clear that in the LSCO samples studied here, the ZF-μSR relaxation is predominantly due to the host nuclei, since the ZF-μSR signal is essentially temperature independent. The following sections are dedicated to modeling the ZF-μSR muon spin depolarization caused by the surrounding host nuclei.

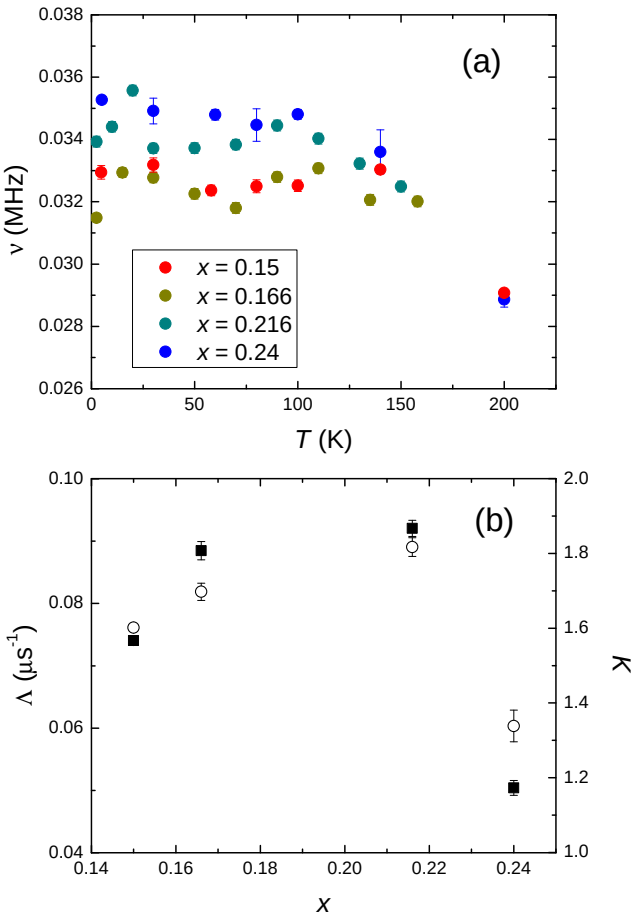

Figure 5.4: Results of fits to Eq. (5.1). (a) Temperature dependence of ν for the 4 different samples. (b) Dependence of the relaxation rate Λ (solid squares) and the exponent K (open circles) on Sr content x. Note both Λ and K are temperature independent fit parameters.

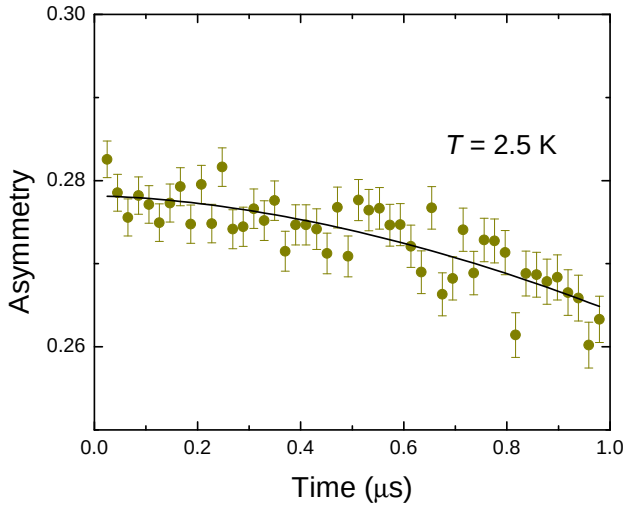

Figure 5.5: The early time ZF-μSR signal of the $x = 0.166$ LSCO single crystal at $T = 2.5$ K shown over the first 1 μs. The solid curve is a fit to the relaxation function of Eq. (5.1).

5.3 Theoretical Model

Here a system where the μ^+ couples to N surrounding nuclear spins I of the host material via dipolar and quadrupolar interactions is considered. Furthermore, the nuclear spins interact amongst themselves via the dipolar interaction and are coupled to the crystal electric field via quadrupolar interactions. The sum of these interactions is described by the following Hamiltonian in SI units [72, 96, 98]

$$H = \sum_{j=1}^{N} H_j = \sum_{j=1}^{N} (H_j^D + H_{\mu j}^Q + H_{oj}^Q) + \sum_{i,j} H_{ij}^{nn}, \tag{5.2}$$

where

$$H_j^D = \hbar\omega_j^D [\mathbf{S}\cdot\mathbf{I}_j - 3(\mathbf{S}\cdot\mathbf{n}_j)(\mathbf{I}_j\cdot\mathbf{n}_j)], \tag{5.3}$$

and

$$H_{\mu j}^Q = \hbar\omega_\mu^Q [(\mathbf{I}_j\cdot\mathbf{n}_j)(\mathbf{I}_j\cdot\mathbf{n}_j) - I_j(I_j+1)/3], \tag{5.4}$$

and

$$H_{ij}^{nn} = \frac{\mu_o}{4\pi}\frac{\hbar^2\gamma_{Ii}\gamma_{Ij}}{r_{ij}^3}[\mathbf{I}_i\cdot\mathbf{I}_j - 3(\mathbf{I}_i\cdot\mathbf{n}_{ij})(\mathbf{I}_j\cdot\mathbf{n}_{ij})]. \tag{5.5}$$

In the above equations H_j^D is the dipole-dipole interaction between the μ^+ and the j^{th} nucleus, with the j^{th} dipolar coupling constant defined as

$$\hbar\omega_j^D = \frac{\mu_o}{4\pi}\frac{\hbar^2\gamma_\mu\gamma_I}{r_j^3}. \tag{5.6}$$

In the above equations $\mathbf{n}_j$ is the unit vector pointing in the direction along the straight line that connects the muon to the j^{th} nucleus located a distance r_j away, and γ_μ and γ_I are the gyromagnetic ratios of the muon and nuclei, respectively. The interaction term $H_{\mu j}^Q$ is associated with the quadrupolar energy of the nuclear spin I_j due to the electric field gradient (EFG) generated by the positive muon charge. Assuming that there is no screening of the positive muon charge by free charge carriers, the quadrupolar coupling coefficient for the j^{th} nucleus is given by [66]

$$\hbar\omega_{\mu j}^Q = -\frac{1}{4\pi\varepsilon_o}\frac{3e^2Q_j}{2I_j(2I_j-1)}\frac{1}{r_j^3}, \tag{5.7}$$

where Q_j is the nuclear quadrupolar moment. Note that $\omega_{\mu j}^Q$ is dependent on the muon-nucleus separation via the factor $1/r_j^3$.

The term H_{oj}^Q in Eq. (5.2) represents the quadrupolar coupling of the j^{th} nucleus to the crystal EFG. This term appears in the Hamiltonian only if the symmetry of the surrounding charge density around the nucleus is non-cubic, otherwise the net EFG at the nucleus vanishes. Consequently, for materials in which there is cubic symmetry, such as pure copper, H_{oj}^Q is zero. However, in crystals with an inhomogeneous charge distribution, H_{oj}^Q can be the dominant contribution to the quadrupolar interaction. This is the case in LSCO. The explicit form of H_{oj}^Q for LSCO will be shown later.

The last term H_{ij}^{nn} in Eq. (5.2) describes the dipolar interaction between nuclear spins I_i and I_j. In Eq. (5.5) $\mathbf{n}_{ij}$ is the unit vector pointing along the straight line between the i^{th} nucleus and the j^{th} nucleus. As will be shown later, since $\gamma_I < 0.1\gamma_\mu$ for both the Cu and La nuclei, H_{ij}^{nn} has little effect on the muon spin relaxation over the ~ 10 μs time range considered, and therefore can be neglected [98].

5.4 Exact Calculation

For simplicity, in this section we consider a system where the quadrupolar coupling of the nuclei to the crystal EFG is zero, *i.e.* $H_{oj}^{Q}=0$ in Eq. (5.2). Calculations with $H_{oj}^{Q}\neq 0$ will be presented later for the case of LSCO.

In order to perform the calculation we use the matrix representation of the Hamiltonian H. Since each surrounding nucleus has a total spin of I_j, the matrix representation of its spin operator will have dimension $D_j = 2I_j + 1$. Hence H of the entire coupled system, including the $S = 1/2$ muon and N nuclei, will have $D = 2\prod_{j=1}^{N}(2I_j+1)$ basis states. The $D \times D$ Hamiltonian is then diagonalized to obtain its D eigenvalues E_j and the $D \times D$ unitary matrix U containing the corresponding eigenstates.

In our problem the incoming muon spins are fully polarized, as is essentially the case in the experiments the calculations will be compared to. We take the initial muon spin polarization orientation to be directed along the $+\hat{z}$-axis, and define this as the quantization axis. The initial nuclear spin configurations are unknown, but each possible configuration is equally probable. The density matrix formalism is used, where the $D \times D$ density matrix at time zero $\rho(0)$ is initialized such that it represents an ensemble of the system with fully polarized muon spins and unpolarized nuclear spins,

$$\rho(0) = \frac{1}{2}\frac{(1+\sigma_{\mu}^{z})}{\prod_{j}^{N}(2I_j+1)}, \tag{5.8}$$

where $\sigma_{\mu}^{z} = 2S^{z}$ is the z component of the Pauli spin matrices. The time evolution of the measured muon spin polarization along the +z direction is therefore given by

$$P(t) = \mathrm{Tr}[e^{\frac{-iHt}{\hbar}}\rho(0)e^{\frac{iHt}{\hbar}}\sigma_{\mu}^{z}]. \tag{5.9}$$

In general it is tedious difficult to represent the operator $\exp(-iHt/\hbar)$ in matrix form. However, if we transform the Hamiltonian into its basis of eigenstates, then

$$e^{\frac{-iHt}{\hbar}} = Ue^{\frac{-iH^{ei}t}{\hbar}}U^{\dagger}. \tag{5.10}$$

Here U is a unitary matrix which defines a unitary transformation of H, $\exp(-iH^{ei}t/\hbar)$ is a diagonal matrix with the exponentials of the eigenvalues E_i on its diagonal. Therefore

Eq. (5.9) can be expressed as

$$\begin{aligned} P(t) &= \mathrm{Tr}[Ue^{\frac{-iH^{ei}t}{\hbar}}U^{\dagger}\rho(0)Ue^{\frac{iH^{ei}t}{\hbar}}U^{\dagger}\sigma_{\mu}^{z}] \\ &= \mathrm{Tr}[e^{\frac{-iH^{ei}t}{\hbar}}U^{\dagger}\rho(0)Ue^{\frac{iH^{ei}t}{\hbar}}U^{\dagger}\sigma_{\mu}^{z}U] \\ &= \mathrm{Tr}[e^{\frac{-iH^{ei}t}{\hbar}}\rho^{'}(0)e^{\frac{iH^{ei}t}{\hbar}}\sigma_{\mu}^{z'}], \end{aligned} \tag{5.11}$$

where $\rho^{'}(0) = U^{\dagger}\rho(0)U$ and $\sigma_{\mu}^{z'} = U^{\dagger}\sigma_{\mu}^{z}U$ are the initial density matrix and the z-component Pauli spin matrix represented in the basis of eigenstates, respectively.

We now outline a scheme for constructing the matrix representations of the Hamiltonian of Eq. (5.2). For the j^{th} nucleus with a total spin of I_j, there are $D_j = 2I_j + 1$ eigenstates of $\hat{I}_z$, which can be arranged in descending order of their eigenvalues and represented by a set of D_j column vectors $\{w^{q_j}\}$, where $q_j = 1,2,...,D_j$ for each nucleus indexed by $j = 1,2,...,N$. The column vectors have length D_j and entries $w_{\alpha}^{q_j} = \delta_{\alpha,q_j}$, where $\alpha = 1,2,3,...,D_j$, such that w^{q_j} represents the j^{th} nucleus with z component of spin $I_j - (q_j - 1)$. In addition, the muon eigenstates can similarly be represented as a set of two column vectors, $\{w^{q_\mu}\}$, where $q_\mu = 1,2$.

The basis of the entire coupled spin system can be written as the direct product of the bases of the individual spin systems using the Kronecker product of the matrices given by

$$(A \otimes B)_{rs} = A_{ij}B_{kl}\,, \tag{5.12}$$

where A has dimensions $m \times n$, B has dimensions $u \times v$, $r = u(i-1)+k$ and $s = v(j-1)+l$. Hence the matrix $(A \otimes B)$ has dimensions $mu \times nv$. The basis of the system is then taken as

$$w^{k} = w^{q_\mu} \otimes \left(\otimes_{j=1}^{N} w^{q_j}\right)\,, \tag{5.13}$$

and ordering the w^k in "lexical order"with respect to the w^{q_j}, k is given by

$$k = (q_\mu - 1)\frac{D}{2}\left[\sum_{j=1}^{N} D_j(q_j - 1)\right]\,. \tag{5.14}$$

The first term in Eq. (5.3) may be expanded as follows

$$\begin{aligned} \mathbf{S}\cdot\mathbf{I}_j &= S_x I_{xj} + S_y I_{yj} + S_z I_{zj} \\ &= \sum_{\alpha}^{x,y,z} S_\alpha I_{\alpha j}\,, \end{aligned} \tag{5.15}$$

where $S_\alpha I_{\alpha j}$ is given by

$$\begin{aligned} S_\alpha I_{\alpha j} &= S_\alpha \otimes II_{D_1} \otimes II_{D_2} \otimes ... \otimes I_{\alpha_j} \otimes ... II_{D_N} \\ &= S_\alpha \otimes \left(\otimes_{i=1}^{j-1} II_{D_i}\right) I_\alpha \left(\otimes_{i=j+1}^{N} II_{D_i}\right), \end{aligned} \tag{5.16}$$

with II_n representing the $n \times n$ identity matrix. The second term in Eq. (5.3) is given by

$$3(\mathbf{S}\cdot\mathbf{n}_j)(\mathbf{I}\cdot\mathbf{n}_j) = 3\left(\sum_\alpha^{x,y,z} n_{\alpha j} S_{\alpha j}\right)\left(\otimes_{i=1}^{j-1} II_{D_i}\right) \otimes \left(\sum_\alpha^{x,y,z} n_{\alpha j} I_{\alpha j}\right) \otimes \left(\otimes_{i=j+1}^{N} II_{D_i}\right). \tag{5.17}$$

The first quadrupolar term in Eq. (5.4) is given by

$$(\mathbf{I}_j\cdot\mathbf{n}_j)(\mathbf{I}_j\cdot\mathbf{n}_j) = II_2 \otimes \left(\otimes_{i=1}^{j-1} II_{D_i}\right) \otimes \left[\left(\sum_\alpha^{x,y,z} n_{\alpha j} I_{\alpha j}\right) \times \left(\sum_\beta^{x,y,z} n_{\beta j} I_{\beta j}\right)\right] \otimes \left(\otimes_{i=j+1}^{N} II_{D_i}\right). \tag{5.18}$$

Finally, the second quadrupolar term in Eq. (5.4) is given by

$$\frac{1}{3} I_j(I_j+1) = \frac{1}{3} I_2 \otimes \left(\otimes_{i=1}^{j-1} II_{D_i}\right) I_j(I_j+1) II_{D_j} \otimes \left(\otimes_{i=j+1}^{N} II_{D_i}\right). \tag{5.19}$$

5.5 Copper: An Archetype

To illustrate the validity of the general assumptions in our calculations, as an example we now proceed to calculate $P(t)$ in copper. In pure copper, which has a face-centred cubic (FCC) crystal structure, the positive muon resides at the octahedral site between 6 Cu atoms. Consequently, we consider a system in which the muon interacts with these 6 nearest neighbour Cu nuclei.

5.5.1 Importance of Quadrupolar Coupling

Figure 5.6(a) shows the time evolution of the muon spin polarization of pure copper at zero field, calculated with and without the quadrupolar term. The quadrupolar interaction has a significant effect on the muon spin relaxation. Figure 5.6(b) shows a comparison of $P(t)$ for two different orientations of the initial muon spin polarization $\mathbf{P}(0)$. In copper, $P(t)$ displays little dependence on the initial muon spin orientation. Assuming the lattice constant $a = 3.61$ Å of copper is unaffected by the presence of the positive muon, and that

Particle/Nuclei	**Natural Abundance**	**Spin**	γ rad ·MHz/T	Q $10^{-30}\mathrm{m}^{-1}$	ω_o^Q MHz
μ^+	N/A	1/2	851.616	N/A	N/A
^{63}Cu	69.17%	3/2	71.118	-22	213.6
^{65}Cu	30.83%	3/2	76.044	-20.4	194.8
^{139}La	99.91%	7/2	38.083	20.0	40.2

Table 5.1: Parameters used in the calculations. γ is the gyromagnetic ratio and Q is the nuclear quadrupolar moment. In calculations, γ_{Cu} and Q_{Cu} are weighted averages of the values of the two isotopes, accounting for their different natural abundances. Note that since ^{139}La has near 100% abundance, the contribution of ^{138}La is ignored. The quadrupolar coupling frequency due to the crystal electric field gradient of a particular nuclear species is $\omega_o^Q = 2\pi\nu_Q$, where the values of ν_Q are taken from Nuclear Quadrupolar Resonance (NQR) experiments [96, 97].

there is no screening of the muon charge, Eq. (5.7) gives a quadrupolar coupling frequency of $\omega_\mu^Q = 4.0$ MHz, whereas ω_μ^Q determined by experiment is 3.2 MHz [98]. Nevertheless, the calculated $P(t)$ for copper is not dependent on whether one assumes the calculated or experimental value of ω_μ^Q, as shown in Fig. 5.6(c). In pure copper the dipolar coupling frequency $\omega_D = 0.11$ MHz $\ll \omega_\mu^Q$. In general one expects that the muon spin relaxation will be independent of ω_μ^Q as long as $\omega_\mu^Q/\omega_D \gg 1$. Consequently, the assumption of no charge screening on the positive muon is appropriate here. However, if $\omega_\mu^Q/\omega_D \sim 1$, the dipolar and quadrupolar contributions are both relevant, leading to substantially different forms of $P(t)$, as is demonstrated in Fig. 5.6(c).

5.5.2 Omission of Nuclear-Nuclear Dipolar Interaction

The dipolar interaction among the nuclear spins H^{nn} was omitted in the calculations shown above, because $\gamma_I < 0.1\gamma_\mu$. This approximation is verified in Fig. 5.7, which shows very similar $P(t)$ curves calculated with and without H^{nn}. Consequently, H^{nn} is neglected in the forthcoming calculations.

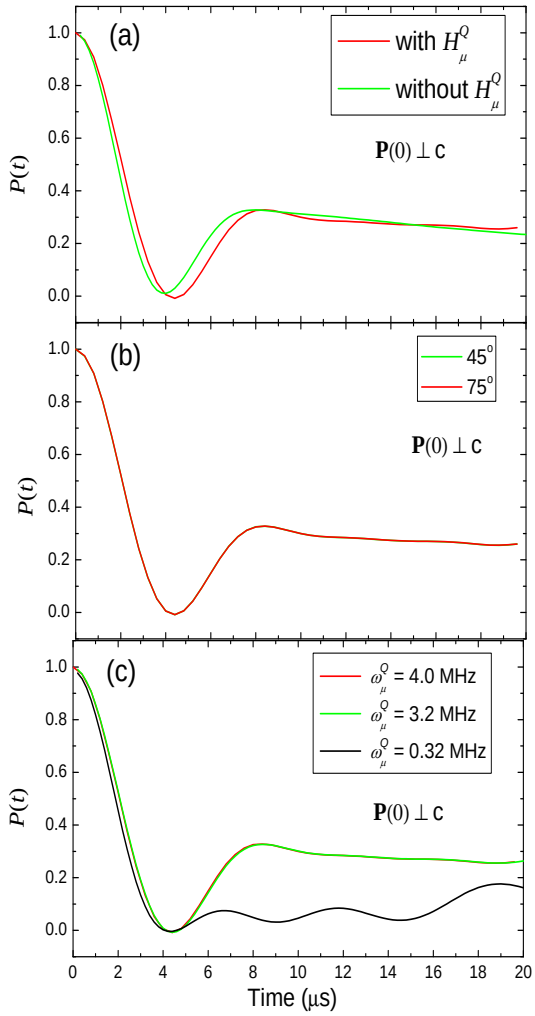

Figure 5.6: Calculated muon spin relaxation function $P(t)$ for μ^+ in pure copper, with the muon residing at the octahedral interstitial site of the FCC crystal structure. In all calculations shown here, the initial muon spin polarization $\mathbf{P}(0)$ is perpendicular to the crystallographic $\hat{c}$-axis, and the muon interactions are with the six nearest neighbouring Cu nuclear spins. (a) Comparison of $P(t)$ calculated with (red curve) and without (green curve) the quadrupolar interaction H_μ^Q between the μ^+ and the nuclear spins. (b) Comparison of $P(t)$ for initial muon spin polarization $\mathbf{P}(0)$ oriented 45° (green) and 75° (red) with respect to the crystallographic $\hat{a}$-axis. (c) $P(t)$ for different values of the quadupolar coupling frequency ω_μ^Q. Note that the black curve corresponds to an ω_μ^Q that is comparable to the dipolar coupling frequency ω_D, with $\omega_\mu^Q/\omega_D \sim 3$.

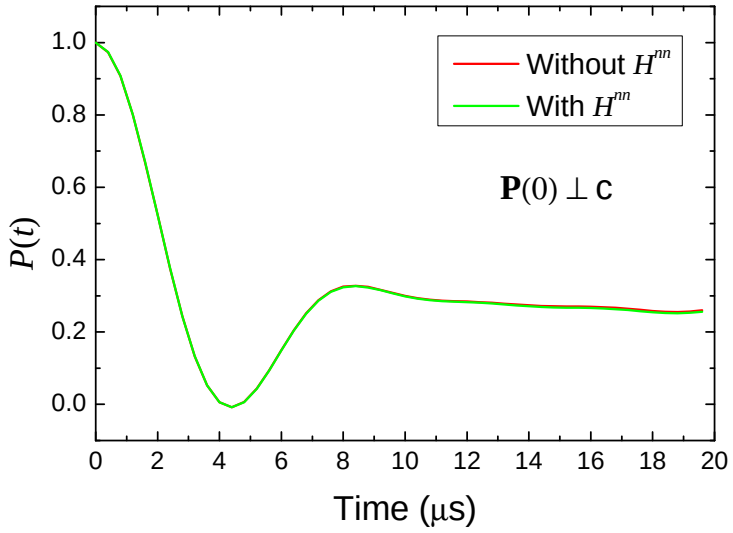

Figure 5.7: Calculated muon spin relaxation function for pure copper, with and without the dipolar interaction H^{nn} among nuclear spins.

5.6 Approximate Calculation

Determining $P(t)$ involves calculating the eigenvalues and eigenvectors of the Hamiltonian matrix with dimension $D = 2\prod_j^N (2I_j + 1)$. For the calculations in Cu in the last section, $D =$ 8192. The dimension D evolves exponentially as the number of nuclei included increases, making this exact calculation unfeasible as N becomes too large. We therefore resort to a technique developed by Celio [98] to study $P(t)$ in pure copper, which is based on the Trotter formula and random phase approximation.

The Trotter formula for a set of Hermitian operators A_j $(j = 1, 2, ...n)$ is given by

$$\exp(A_1 + A_2 + ... + A_n) = \lim_{k\to\infty} [\exp(A_1/k)\exp(A_2/k)\cdots\exp(A_n/k)]^k . \tag{5.20}$$

Here k is an integer and is chosen to be large enough to ensure convergence. Using Eq. (5.20), the time evolution operator $\exp(-iHt/\hbar)$ in Eq. (5.9) can be expressed as

$$\begin{aligned}\exp(-iHt/\hbar) &= \exp\left(-i\sum_{j=1}^{N} H_j t/\hbar\right) \\ &= \lim_{k\to\infty} [\exp(-iH_1 t/\hbar k)\exp(-iH_2 t/\hbar k)\cdots\exp(-iH_N t/\hbar k)]^k . \end{aligned} \tag{5.21}$$

Since the Hamiltonian H_j involves only the muon spin and a single nuclear spin, it therefore has dimension $D_j = 2I_j(I_j+1)$. This Hamiltonian acts only on a small subspace (of dimension D_j) of the basis of the total Hamiltonian H. Consequently, in Eq. (5.21) one just has to diagonalize the smaller N different Hamiltonians H_j and multiply the results accordingly. The precision of the approximation is determined by the number of multiplications k.

To circumvent computing storage limitations, we choose to work in the *Schrödinger* representation. For convenience, we use a different notation to denote the basis in Eq. (5.13) as $|\psi_m\rangle$. The time evolution of the basis obeys

$$\begin{aligned} |\psi_m(t)\rangle &= \exp(-iHt/\hbar)\,|\psi_m(0)\rangle \\ &= \lim_{k\to\infty}[\exp(-iH_1t/\hbar k)\exp(-iH_2t/\hbar k)\cdots \\ &\quad \cdots\exp(-iH_Nt/\hbar k)]^k\,|\psi_m(0)\rangle\ . \end{aligned} \tag{5.22}$$

The problem of calculating $P(t)$ is now re-expressed as follows [98]

$$P(t) = \sum_m^{D/2} w_m \langle\psi_m(t)\,|\sigma^z|\,\psi_m(t)\rangle\,, \tag{5.23}$$

where $w_m = 2/D$ is the probability of starting from one initial pure basis $|\psi_m(0)\rangle$ with the muon spin directed along the $+\hat{z}$-axis. The above equation involves calculating $\langle\sigma^z\rangle$ with $D/2$ different initial states, which requires too much computing time. However, this problem can be avoided by using a method similar to the random-phase approximation [101]. The initial state of the system is chosen as follows

$$|\phi(0)\rangle = \sum_{m=1}^{D/2}(2/D)^{1/2}e^{i\lambda_m}\,|\psi_m(0)\rangle\,, \tag{5.24}$$

where each phase λ_m is taken to be random. This state evolves with time according to

$$|\phi(t)\rangle = \sum_{m=1}^{D/2}(2/D)^{1/2}e^{i\lambda_m}\,|\psi_m(t)\rangle\,. \tag{5.25}$$

Consequently, the muon spin polarization $P(t)$ is given by

$$\begin{aligned} P(t) &= \langle \phi(t) | \sigma^z | \phi(t) \rangle \\ &= \sum_{m=1}^{D/2} \frac{2}{D} \langle \psi_m(t) | \sigma^z | \psi_m(t) \rangle + \sum_{\substack{m,n=1, \\ m \neq n}}^{D/2} \frac{2}{D} e^{i(\lambda_m - \lambda_n)} \langle \psi_n(t) | \sigma^z | \psi_m(t) \rangle \, . \end{aligned} \tag{5.26}$$

The first term in the last equation is equal to Eq. (5.23), while the second term converges to zero at large D, as the random phases of different initial basis states interfere destructively. We therefore obtain a solution that is fairly close to the precise calculation.

To test the applicability of this approximation method, we again consider muon spin relaxation in pure copper. The parameters used are the same as those in the exact calculation. In real calculations, the accuracy of the approximated $P(t)$ depends on the time increment, $\Delta t = t/k$ in Eq. (5.21) for each step. To ensure good agreement with the exact calculation, Δt must be sufficiently smaller than the muon relaxation time scale. For the systems studied here with a typical relaxation time scale of the order of ~ 10 μs, we find that $\Delta t = 0.2$ μs is sufficient to guarantee good agreement with the exact calculation and the experimental results (see Fig. 5.8).

5.7 $La_{2-x}Sr_xCuO_4$

5.7.1 Quadrupolar Interaction Due to Crystal EFG

In the above calculations the electric field gradient (EFG) on the nucleus is generated solely by the Coulomb potential of the muon. Since the octahedral site in the crystal lattice of copper has cubic symmetry, there is no EFG created by the crystal to consider. However, in single crystal LSCO, the net EFG due to the crystal is nonzero. This is because LSCO adopts a perovskite structure, with negatively charged copper-oxide layers sandwiched between positively charged lanthanum-oxide layers. In fact, in LSCO, the quadrupolar coupling frequency due to the crystal EFG is of the order of 100 MHz (Table. 5.1), while that due to the EFG of the muon charge is typically smaller than 10 MHz. Consequently, the crystal EFG becomes the dominant contribution to the quadrupolar interactions experienced by the host nuclei, and the H_{oj}^{Q} term in Eq. (5.2) must be included.

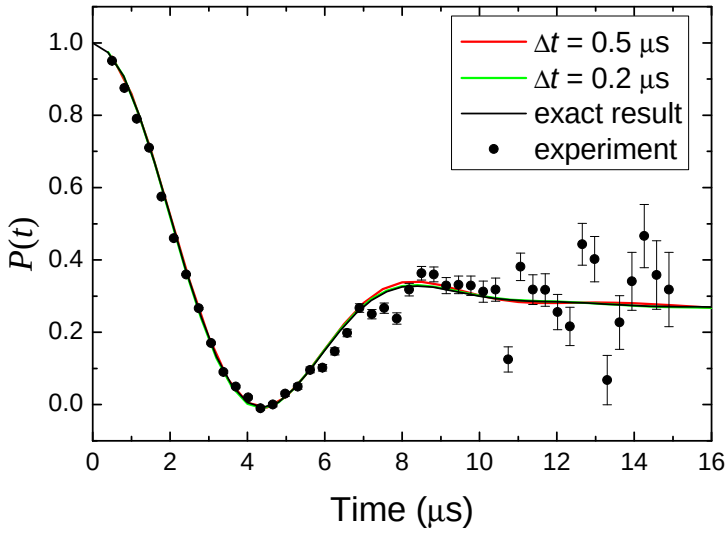

Figure 5.8: Approximate calculation of $P(t)$ for two different Δt's, compared to the exact calculation (black curve) given in Sec. 5.5 and the experimental result [99] (solid points). Note that the experimental data is an average of measurements between $40 \sim 80$ K.

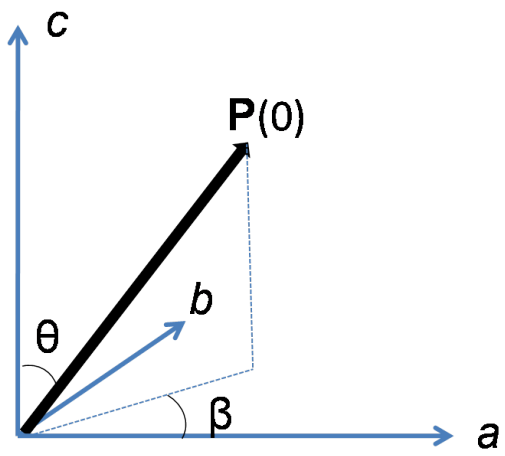

Figure 5.9: Orientation of the initial muon spin polarization $\mathbf{P}(0)$. The $\hat{a}$, $\hat{b}$, and $\hat{c}$ axes are the crystallographic axes of the LSCO crystal structure shown in Fig. 5.10(b).

Recall that H_{oj}^{Q} is the quadrupolar coupling of the j^{th} nucleus to the crystal EFG, which in LSCO is given by [72, 96]

$$H_{oj}^{Q} = \frac{\hbar\omega_{oj}^{Q}}{2}\left[I_{jz}^{2} - \frac{1}{3}I_{j}(I_{j}+1) + \frac{1}{6}\eta(I_{j+}^{2} + I_{j-}^{2})\right], \tag{5.27}$$

where ω_{oj}^{Q} is the quadrupolar coupling frequency given in Table. 5.1, and η is the asymmetry parameter associated with the symmetry of the EFG around the nucleus. In particular, $\eta = 0$ corresponds to full axial symmetry. Due to the tetragonal crystal symmetry, the crystal EFG of LSCO has high axial symmetry with respect to crystallographic $\hat{c}$-axis (see Fig. 5.10(b)). For the Cu sites, $\eta = 0.03$ [100], while for La, $\eta = 0.02$ [97].

In Eq. (5.27) the $\hat{c}$-axis is the quantization axis, which is parallel to $\hat{z}$. Consequently, with the direction of initial muon spin polarization at a polar angle θ and azimuthal angle β with respect to the crystal crystallographic axes as shown in Fig. 5.9, the initial muon spin state is denoted by $\left(\cos\frac{\theta}{2}e^{-i\beta/2}, \sin\frac{\theta}{2}e^{i\beta/2}\right)^{T}$. Hence, similar to Eq. (5.13), the complete initial state of the Hamiltonian for a particular initial nuclear spin configuration becomes

$$|\psi_{m}(0)\rangle = \left(\cos\frac{\theta}{2}e^{-i\beta/2}, \sin\frac{\theta}{2}e^{i\beta/2}\right)^{T} \otimes \left(\otimes_{j=1}^{N} w^{q_j,j}\right), \tag{5.28}$$

and the expectation value to be calculated becomes $\langle S' \rangle$, with

$$S' = \sin\theta\cos\beta\, S_x + \sin\theta\sin\beta\, S_y + \cos\theta\, S_z \qquad (5.29)$$
$$= \frac{1}{2}\begin{pmatrix} \cos\theta & \sin\theta e^{-i\beta} \\ \sin\theta e^{i\beta} & -\cos\theta \end{pmatrix}.$$

5.7.2 General Considerations

Having demonstrated the efficiency and accuracy of the approximation method in determining the muon spin relaxation function $P(t)$, we now use this method to calculate $P(t)$ in single crystal LSCO. The parameters used in the following calculations are given in Table 5.1. Note that the Sr nuclei are not included in the interactions. This is because among the four stable isotopes of Sr, only ^{87}Sr has nonzero spin. Furthermore, although ^{87}Sr has spin $I = 9/2$, its natural abundance is only 7% and in LSCO less than $\sim 15\%$ of the La are substituted with Sr. This is consistent with ZF-μSR measurements of LSCO single crystals presented here and by MacDougall *et al.* [40], which do not show an appreciable dependence on Sr content. Note that the weak temperature dependence shown below $x \sim 0.22$ in Fig. 5.4(b) may be partially due to changes in the lattice constants with substitution of La with the smaller Sr atom. Nevertheless, the calculations here are performed under the assumption of the muon residing in a single crystal of the parent compound La_2CuO_4. In addition, for Sr content above $x \approx 0.15$, the electronic moments of the Cu atoms are rapidly fluctuating outside the μSR time window [105], making their contributions to the muon spin relaxation negligible. Consequently, the electronic moments of Cu are neglected in the calculations shown below.

Only nearest-neighbour nuclei are considered in the calculation, as nuclei located further away from the muon have little effect on the muon spin relaxation in the μSR time range of $\sim 10\ \mu$s. This is demonstrated in Fig. 5.10(a), where $P(t)$ has been calculated for the muon sites B_a and B_b (see Table 5.2). Both B_a and B_b correspond to the same muon site and initial muon spin polarization $\mathbf{P}(0)$, but with the latter including three additional Cu nuclei located at distances further away from the muon.

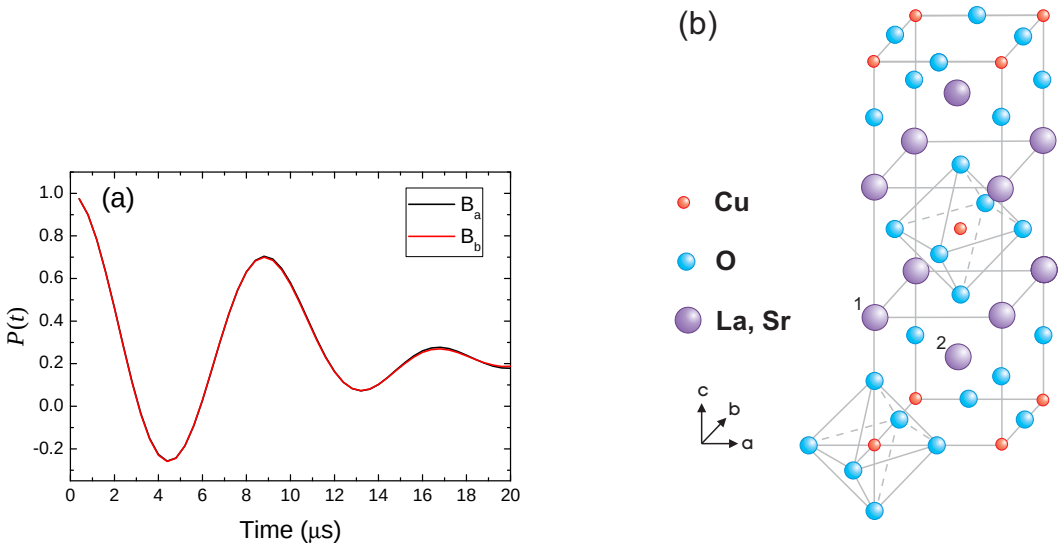

Figure 5.10: (a) Muon spin relaxation function $P(t)$ for the same muon site and $\mathbf{P}(0)$, but taking into account a different number of nuclei (see Table. 5.2 for explanation of the sites B_a and B_b). (b) Tetragonal unit cell of LSCO. The La atoms at different sites are distinguished by numerical labels 1 and 2. The lattice constants reported by Radovic *et al.* [102] are $a = 3.80$ Å , $b = 3.80$ Å and $c = 13.12$ Å . Note that slightly different values of the lattice constants are reported by different experiments on different samples. Yet these differences pose little effect on the results. In addition, a and b are treated as equivalent given that even in the tetragonal phase they differ by only 1%.

The experimentally observed ZF-μSR spectra suggest a rather weak dependence of $P(t)$ on the direction of the initial muon spin polarization $\mathbf{P}(0)$ in the *ab* plane, when $\mathbf{P}(0)$ is perpendicular to the crystallographic $\hat{c}$-axis. However, in the calculations here, the strength of the dependence of $P(t)$ on the direction of $\mathbf{P}(0)$ is found to vary significantly for different muon sites, as is shown in Fig. 5.12. The variation of $P(t)$ for different orientations of $\mathbf{P}(0)$ in the *ab* plane is negligible only at muon sites that are highly symmetric with respect to the crystal lattice, such as the $(0,0,z)$ site (see Fig. 5.11). This is similar to the situation in Fig. 5.6 where the muon in copper is located at the symmetrical octahedral site.

Experimentally, a much slower muon spin relaxation is observed in ZF-μSR measurements on LSCO when $\mathbf{P}(0) \parallel \hat{c}$ [40]. This is consistent with the calculations here, as shown in Figs. 5.11 and 5.12. Since $P(t)$ for the case $\mathbf{P}(0) \parallel \hat{c}$ does not dip below zero, the ZF-μSR spectra for this orientation can be fit with the static Gaussian Kubo-Toyabe function. The dependence of $P(t)$ on the muon site for $\mathbf{P}(0) \parallel \hat{c}$ or $\mathbf{P}(0) \perp \hat{c}$ means that the ZF-μSR signal can be used to determine the muon site in LSCO, provided that there is only a single muon site, the muon does not diffuse, and there are no other sources of relaxation (*e.g.* electronic moments and/or loop-current order).

One might expect a muon site that is symmetric with respect to the electrostatic Coulomb potential of the crystal. However, for muon sites (x,x,z) where $x \neq 0$, $P(t)$ for the case $\mathbf{P}(0) \perp \hat{c}$ changes significantly as the orientation of the initial muon spin polarization is varied within the *ab* plane (see Fig. 5.12(a)). This seems inconsistent with our experiments, where the orientation of $\mathbf{P}(0)$ in the *ab* plane was certainly different for certain measurements on the same single crystal, but the ZF-μSR spectra looked similar. The calculations here show that the $P(t)$ for various directions of the initial muon spin polarization in the *ab* plane begin to converge as the muon is positioned closer to the *ac* plane (compare Figs. 5.12(a), (b) and (c)). Consequently, our search for possible muon sites here is restricted to the *ac* plane. This agrees with a ZF-μSR study of the parent compound of La_2CuO_4 by Hitti *et al.* [103], where muon sites out of the *ac* plane were ruled out due to the absence of the observation of two oscillatory components in the ZF-μSR spectra.

Comparing Figs. 5.12(c) and (d), one can see that as the muon site is moved along the $\hat{a}$ direction towards the centre of the *ac* plane, the muon spin relaxation becomes faster for the case $\mathbf{P}(0) \parallel \hat{c}$. Furthermore, as can be seen in Figs. 5.12(c), (e) and (f), although moving the muon from site X3 to site X6 (see Table 5.2) in the direction of the $\hat{c}$-axis retains the

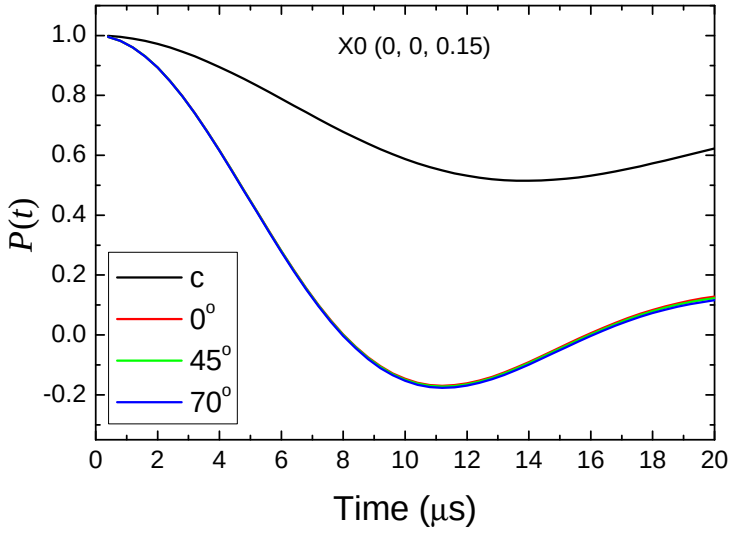

Figure 5.11: Dependence of the muon spin relaxation function on the direction of the initial muon spin polarization $\mathbf{P}(0)$ for the muon site X0 given in Table. 5.2. The solid curves correspond to the cases with $\mathbf{P}(0) \perp \hat{c}$. The labels indicate the angles between $\mathbf{P}(0)$ and the crystallographic $\hat{a}$-axis. The black curves correspond to $\mathbf{P}(0) \parallel \hat{c}$.

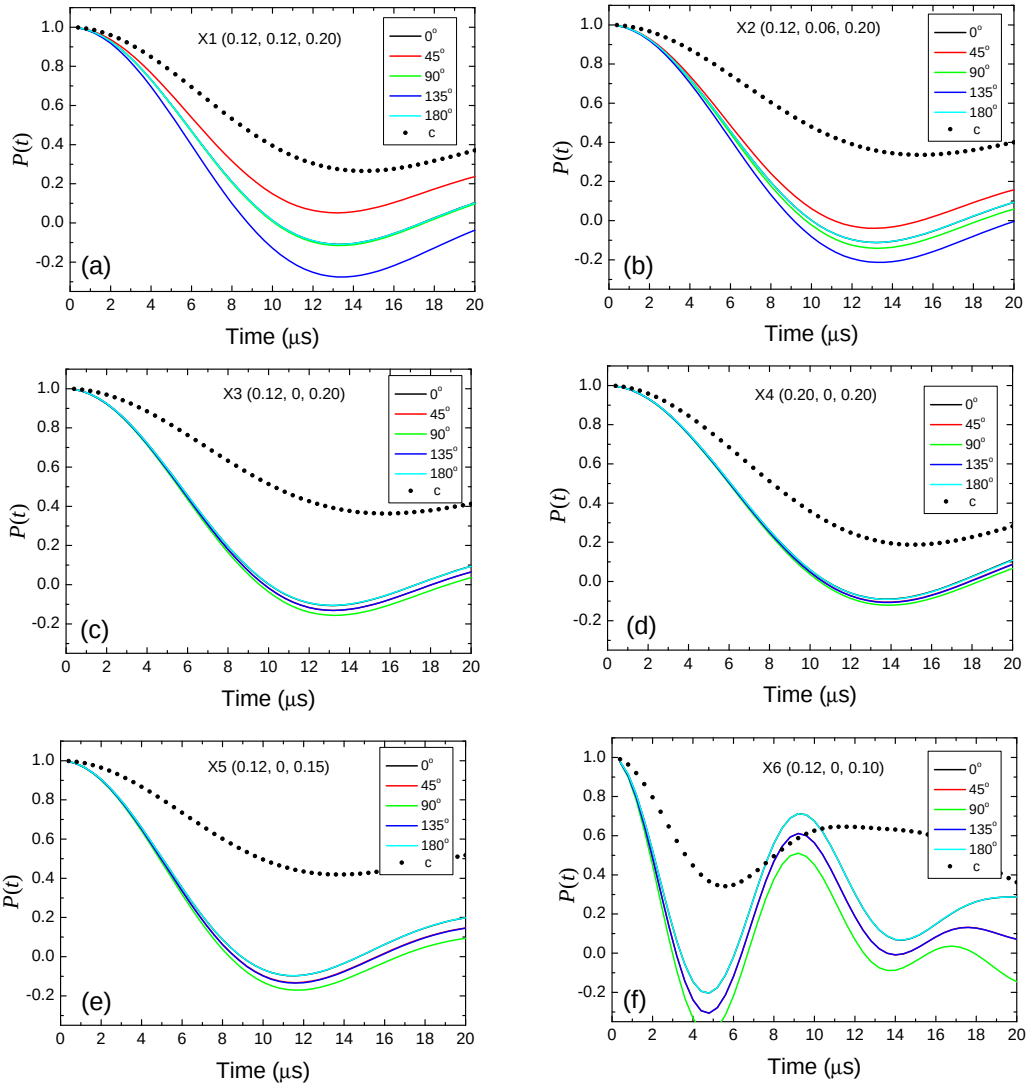

Figure 5.12: Dependence of the muon relaxation function on the initial muon spin polarization $\mathbf{P}(0)$ for various muon sites. The solid curves correspond to the cases with $\mathbf{P}(0) \perp \hat{c}$, the labels indicate the angles between the direction of $\mathbf{P}(0)$ and the crystallographic $\hat{a}$-axis. The dotted curves correspond to $\mathbf{P}(0) \parallel \hat{c}$. The muon sites are given in Table. 5.2.

Label	Muon Site	Nuclei Included in Calculation
M	(0.5, 0.0, 0.096)	2Cu, 2La(2)
T1	(0.2, 0.0, 0.15)	2Cu, La(1), 2La(2)
T2	(0.225, 0.0, 0.225)	2Cu, La(1), 2La(2)
U1	(0.12, 0, 0.11)	2Cu, La(1), 2La(2)
B_a	(0.1, 0.0, 0.1)	Cu, La(1), 2La(2)
B_b	(0.1, 0.0, 0.1)	4Cu, La(1), 2La(2)
X0	(0.0, 0.0, 0.15)	1Cu, La(1), 4La(2)
X1	(0.12, 0.12, 0.20)	3Cu, La(1), 4La(2)
X2	(0.12, 0.06, 0.20)	3Cu, La(1), 4La(2)
X3	(0.12, 0, 0.20)	2Cu, La(1), 4La(2)
X4	(0.20, 0, 0.20)	2Cu, La(1), 4La(2)
X5	(0.12, 0, 0.15)	2Cu, La(1), 4La(2)
X6	(0.12, 0, 0.10)	2Cu, La(1), 4La(2)
A	(0.0, 0.0, 0.212)	5Cu, La(1), 4La(2)

Table 5.2: Muon sites corresponding to the polarization functions plotted in the main text, where the muon site coordinates are denoted in units of the lattice constants. The indicated atoms correspond to the ones that are closest to the muon site. Note we denote two Cu nuclei as 2Cu, and a La nucleus at site 1 as La(1), etc.

slower relaxation for $\mathbf{P}(0) \parallel \hat{c}$, a strong dependence on the orientation of $\mathbf{P}(0)$ in the *ab* plane re-appears when $\mathbf{P}(0) \perp \hat{c}$. Finally, a pronounced oscillation is seen in $P(t)$ for site X6 and the minimum of $P(t)$ shifts toward earlier times. This is the case when the muon is located closer to a single nucleus, whose effect dominates.

5.7.3 Results and Discussion

Although there have been several attempts to determine the precise location of the positive muon in single crystal LSCO [103, 104], there is still no general consensus on its location. Figure 5.13 shows $P(t)$ calculated for potential muon sites in the *ac* plane that have been considered in previous studies [103, 104]. However, as is shown in Fig 5.13, none of these

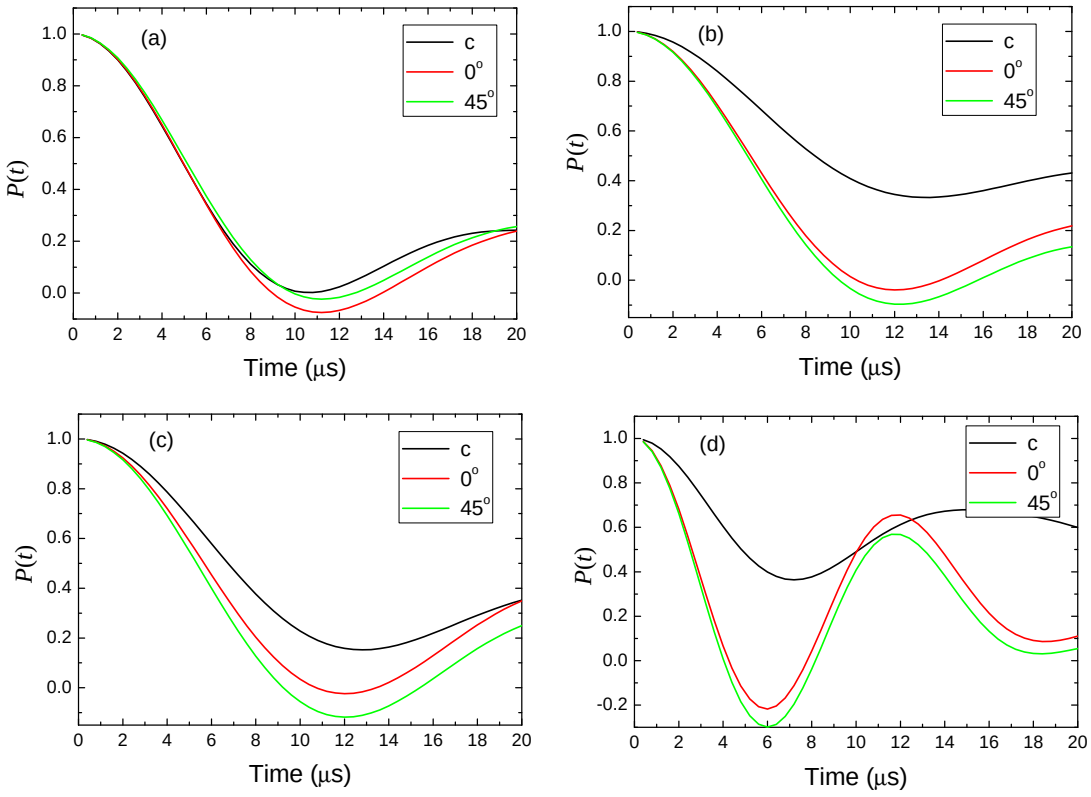

Figure 5.13: Calculated $P(t)$ for various muon sites (a) M, (b) T1, (c) T2, (d) U1, determined by earlier studies [103, 104] (See Table. 5.2). Note that $P(t)$ for $\mathbf{P}(0) \parallel \hat{c}$ are shown in black curves. The red and blue curves correspond to the case $\mathbf{P}(0) \perp \hat{c}$, with $\mathbf{P}(0)$ oriented at angles 0° (red) and 45° (green) with respect to the crystallographic $\hat{a}$-axis.

muon sites generate a muon spin relaxation function that resembles the ZF-μSR signal observed in LSCO for Sr content above $x \approx 0.15$. In particular, the calculated $P(t)$ all exhibit considerable dependence on the direction of $\mathbf{P}(0)$, and in the case of $\mathbf{P}(0) \perp \hat{c}$, $P(t)$ does not dip low enough below zero and does not cross zero at $\sim$ 8 μs, as observed experimentally.

Calculations were performed for many other muon sites. Of the muon sites considered, muon site A (0, 0, 0.212) (see Table. 5.2) agrees best with the ZF-μSR spectra. Figure 5.14 shows the calculated $P(t)$ for muon site A with $\mathbf{P}(0) \perp \hat{c}$, together with the observed ZF-μSR signal in the LSCO samples. Also shown in Fig. 5.14 is $P(t)$ for the case $\mathbf{P}(0) \parallel \hat{c}$ (dotted curves), which relaxes slower than when $\mathbf{P}(0) \perp \hat{c}$. This is consistent with what was observed in the ZF-μSR study of Ref. [40]. As discussed earlier, for this highly symmetric muon site, $P(t)$ is independent of the direction of the initial muon spin polarization $\mathbf{P}(0)$ in the *ab*-plane when $\mathbf{P}(0) \perp \hat{c}$.

The discrepancy between the calculation and the ZF-μSR signal at $T = 5$ K in Fig. 5.14(a) is probably associated with a slight late time distortion, of which there are several possible origins related to the experimental setup. On the other hand, Fig. 5.14(c) shows a strong deviation of the calculated $P(t)$ for the muon site A from the ZF-μSR signal for the $x = 0.24$ sample. Note this deviation is not restricted to very late times. This is possibly due to the effect of electronic phase separation and/or occurrence of paramagnetic moments in this heavily overdoped sample, as mentioned in Section. 5.2. However, the lack of any significant temperature dependence of the ZF-μSR signal is not compatible with the latter explanation. The deviation most likely originates from two slightly different nuclear dipole contributions associated with two phase separated regions. In this case, the ZF-μSR signal is the sum of two nuclear-dipole relaxation components, each having an amplitude that reflects their volume fraction. Having said this, fast fluctuating paramagnetic moments restricted to one of the phase separated regions can affect the nuclear moments in that region, and hence can indirectly influence the ZF-μSR spectrum.

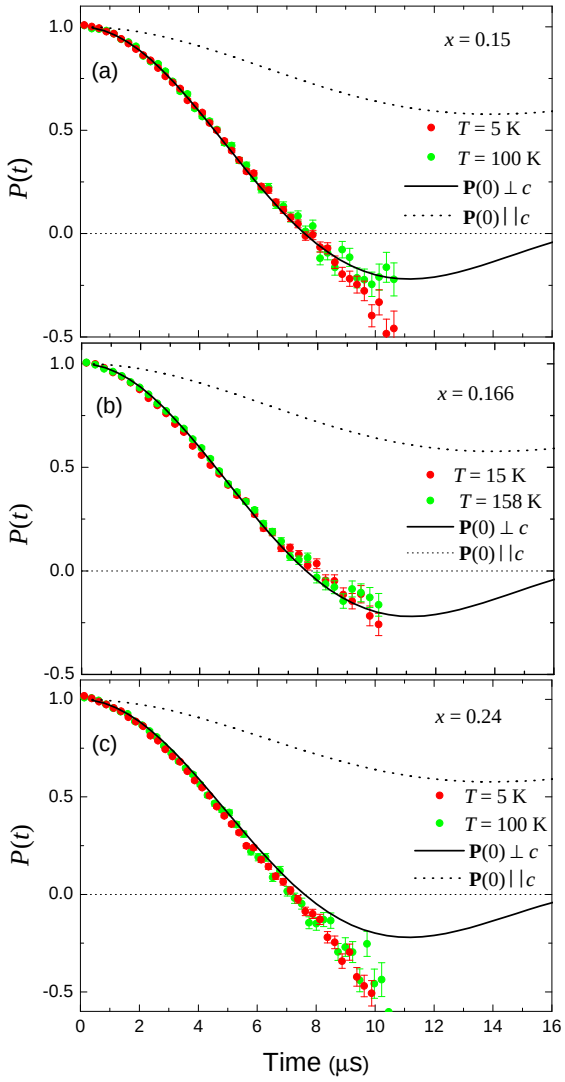

Figure 5.14: Calculated $P(t)$ for muon site A (see Table. 5.2), and ZF-μSR signals for the (a) $x = 0.15$, (b) $x = 0.166$ and (c) $x = 0.24$ single crystals of LSCO. The calculations are shown for the case $\mathbf{P}(0) \perp \hat{c}$ (solid curve) and $\mathbf{P}(0) \parallel \hat{c}$ (dotted curve). Note that the ZF-μSR asymmetry signal is $A(t) = a_o P(t)$. To compare to the calculation of $P(t)$, the experimentally determined amplitude a_o has been divided out. Note that though the calculations were performed considering 5 Cu nuclei that are closest to site A, the same results are obtained even if only the closest Cu nucleus is included.

Chapter 6

Conclusions

This thesis presented TF-μSR measurements of a single crystal of the iron-arsenic superconductor $BaFe_{2-x}Co_xAs_2$ and a ZF-μSR study of single crystals of the cuprate superconductor $La_{2-x}Sr_xCuO_4$, together with theoretical calculations to explain the observed spectra.

The magnetic field distribution $n(B)$ of the vortex state of an overdoped $BaFe_{1.82}Co_{0.18}As_2$ single crystal was measured by TF-μSR, with the aim of determining the temperature dependence of the magnetic penetration depth λ and information on the superconducting pairing symmetry of this material. It was first shown that field-induced magnetism occurs in this material, causing a strong deviation of $n(B)$ from that of the corresponding ideal vortex lattice. Accounting for this magnetism in the analysis of the TF-μSR spectra is non-trivial, because the precise form of the magnetism is unknown. Nevertheless, a simple model of field-induced AFM order was introduced that gives excellent fits of the time spectra under the assumption of weak random frozen disorder of the vortex lattice. Markedly different behaviour for the temperature dependence of λ was obtained compared to results from an analysis that assumed no field-induced magnetism. This demonstrates the difficulty in trying to determine λ in samples where $n(B)$ is strongly influenced by electronic moments.

To simulate the high degree of vortex lattice disorder that is actually observed in $BaFe_{2-x}Co_xAs_2$ and other doped iron-arsenic superconductors, a molecular dynamics method was used to demonstrate the effects of strong disorder on the TF-μSR line shape. The degree of disorder that was assumed in the simulations corresponds to that observed in vortex imaging experiments on $BaFe_{2-x}Co_xAs_2$. The calculated $n(B)$ indicate that strong vortex-

lattice disorder causes a significant broadening of the magnetic field distribution of the ideal vortex lattice. More importantly, because a high-degree of disorder strongly smears out important features of the magnetic field distribution, fits of $n(B)$ to phenomenological models of the vortex lattice are either not possible or unreliable. Strong disorder of the vortex lattice is also expected to significantly modify the overlap of the electronic states of neighbouring vortices, which in turn modifies the spatial dependence of the local magnetic field $B(\mathbf{r})$ between the vortices. Furthermore, significant disorder causes pairbreaking and a corresponding increase of λ. Neither of these effects can be factored out to determine λ in the absence of disorder. Moreover, the effects of severe vortex-lattice disorder cannot be reliably modeled to determine the "true" in the sample.

In the second part of the thesis, high statistics ZF-μSR measurements of $La_{2-x}Sr_xCuO_4$ single crystals at several dopings was reported. The primary motivation of these measurements was to search for local magnetic fields associated with a proposed circulating current phase in the pseudogap region. It was shown that the observed ZF-μSR relaxation is predominantly caused by the randomly oriented nuclear dipole moments of the host material, and no evidence for loop-current order was found. Even so, the ZF-μSR signal in $La_{2-x}Sr_xCuO_4$ cannot be described by the standard static Gaussian Kubo-Toyabe relaxation function which is commonly used to approximate muon spin relaxation due to randomly oriented nuclear dipole moments. To determine the nuclear contribution to the muon spin relaxation, a quantum mechanical model taking into account all of the important interactions between the positive muon, the nuclei and the crystal electric field gradient was presented. At a highly symmetric muon stopping site near the apical O atom directly above the in-plane Cu (see Fig. 5.10(b)), the calculated muon spin relaxation function for $\mathbf{P}(0) \perp \hat{c}$ agrees fairly well with the ZF-μSR spectra observed in the single crystals of $La_{2-x}Sr_xCuO_4$. However, the calculated $P(t)$ for $\mathbf{P}(0) \parallel \hat{c}$ at this same site has a relaxation rate over the first 8 μs that is $\sim 25\%$ slower than what is observed experimentally. Hence an exhaustive test of muon sites near this location still needs to be carried out. A muon that resides directly above an in-plane Cu atom is blind to the loop current pattern shown in Fig. 1.5, as the net dipolar field from the loop currents is zero at such sites. This might explain why the weak magnetic order observed in $La_{1.915}Sr_{0.085}CuO_4$ by polarized neutron scattering [25], which has been considered as evidence for loop-current order, has not been detected by ZF-μSR.

Bibliography

[1] M. Tinkham, *Introduction to Superconductivity*, McGraw-Hill 1996.

[2] F. London and H. London, Proc. R. Soc. London, Ser A **149**, 71 (1935).

[3] J. Bardeen, L.N. Cooper, and J.R. Schrieffer, Phys. Rev., **106**, 162 (1957).

[4] B. Muhlschlegel, Z. Phys. **155**, 313 (1959).

[5] J. Annett, *et al.* Phys. Rev. B **43**, 2778 (1991).

[6] P.J. Hirschfeld, *et al.* Phys. Rev. B **50**, 10250 (1994).

[7] W. Hardy, *et al.* Phys. Rev. Lett. **70**, 3999 (1993).

[8] J.G. Bednorz and K.A. Müller, Z. Phys. B: Condens. Matter **64**, 189 (1986).

[9] A. Damascelli, Z. Hussain, and Z.X. Shen, Rev. Mod. Phys. **75**, 473 (2003).

[10] M.H. Julien, Physica B **329**, 693 (2003).

[11] C. Nidermayer, *et al.*, Phys. Rev. Lett. **80**, 3843 (1998).

[12] S. Wakimoto, *et al.*, Phys. Rev. Lett. **98**, 247003 (2007).

[13] S. Chakravarty, R.B. Laughlin, D.K, Morr, and C. Nayak, Phys. Rev. B **63**, 094503 (2001).

[14] S. Tewari, C. Zhang, V.M. Yakovenko, and S. Das Sarma, Phys. Rev. Lett. **100**, 217004 (2008).

[15] C.M. Varma, Phys. Rev. B **55**, 14554 (1997).

[16] C.M. Varma, Phys. Rev. Lett. **83**, 3538 (1999).

[17] R.H. He, *et al.*, Science **331**, 1579 (2011).

[18] H.A. Mook, P. Dai, and F. Doan, Phys. Rev. B **64**, 012502 (2001).

[19] H.A. Mook, *et al.*, Phys. Rev. B **66**, 144513 (2002).

[20] H.A. Mook, *et al.*, Phys. Rev. B **69**, 134509 (2004).

[21] B. Fauqué, *et al.*, Phys. Rev. Lett. **96**, 197001 (2006).

[22] H.A. Mook, Y. Sidis, B. Fauqué, V. Balédent, and P. Bourges, Phys. Rev. B **78**, 020506(R) (2008).

[23] V. Balédent, *et al.*, Phys. Rev. B **83**, 104504 (2011).

[24] Y. Li, *et al.*, Nature **455**, 372 (2008).

[25] V. Baldent, *et al.*, Phys. Rev. Lett. **105**, 027004 (2010).

[26] A. Kaminski, *et al.*, Nature **416**, 610 (2002).

[27] V. Arpiainen, A. Bansil, and M. Lindroos, **103**, 067005 (2009).

[28] J. Xia, *et al.*, Phys. Rev. Lett. **100**, 127002 (2008).

[29] V. Aji, A. Shekhter, and C.M. Varma, Phys. Rev. B **78**, 094421 (2008).

[30] B. Leridon, P. Monod, D. Colson, and A. Forget, Europhys. Lett. **87**, 17011 (2009).

[31] J.E. Sonier, *et al.*, Science **292**, 1692 (2001).

[32] J.E. Sonier, *et al.*, Phys. Rev. B **66**, 134501 (2002).

[33] V. Aji and C.M. Varma, Phys. Rev. B **75**, 224511 (2007).

[34] C. Weber, A. Lauchli, F. Mila, and T. Giamarchi, Phys. Rev. Lett. **102**, 017005 (2009).

[35] Y. He and C.M. Varma, Phys. Rev. Lett. **106**, 147001 (2011).

[36] J.E. Sonier, *et al.*, Phys. Rev. Lett. **103**, 167002 (2009).

[37] A. Shekhter, L. Shu, V. Aji, D.E. MacLaughlin and C.M. Varma, Phys. Rev. Lett. **101**, 237001 (2008).

[38] S. Strässle, J. Roos, M. Mali, H. Keller, and T. Ohno, Phys. Rev. Lett. **101**, 237001 (2008).

[39] S. Strässle, B. Graneli, M. Mali, J. Roos, and H. Keller, Phys. Rev. Lett. **106**, 097003 (2011).

[40] G.J. MacDougall, *et al.*, Phys. Rev. Lett. **101**, 017001 (2008).

[41] R. Kubo, T. Toyabe, Magnetic Resonance and Relaxation, ed. R. Blinc, North Holland, Amsterdam, 1967.

[42] Y. Kamihara, T. Watanabe, M. Hirano, and H. Hosono, J. Am. Chem. Soc. **130**, 3296 (2008).

[43] J. Paglione and R.L. Greene, Nature Physics **6**, 645 (2010).

[44] M.D. Lumsden and A.D. Christianson, *et al.*, J. Phys.: Condens. Matter **22**, 203203 (2010).

[45] Y.M. Xu, *et al.*, Nat. Commun. **2**, 392 (2011).

[46] M.A. Tanatar, *et al.*, Phys. Rev. Lett. **104**, 067002 (2010).

[47] K. Terashima, *et al.*, Proc. Natl. Acad. Sci. U.S.A. **106**, 7330 (2009).

[48] T. Fischer, *et al.*, Phys. Rev. B **82**, 224507 (2010).

[49] K. Gofryk, *et al.*, Phys. Rev. B **81**, 184518 (2010).

[50] J.K. Dong, *et al.*, Phys. Rev. B **81**, 094520 (2010).

[51] J. Yong, *et al.*, Phys. Rev. B **83**, 104510 (2011).

[52] J.E. Sonier, J.H. Brewer, and R.F. Kiefl, Rev. Mod. Phys. **72**, 769 (2000).

[53] H. Luetkens, *et al.*, Phys. Rev. Lett. **101**, 097009 (2008).

[54] R. Khasanov, *et al.*, Phys. Rev. B **78**, 092506 (2008).

[55] R. Khasanov, *et al.*, Phys. Rev. Lett. **103**, 067010 (2009).

[56] R. Khasanov, *et al.*, Phys. Rev. Lett. **102**, 187005 (2009).

[57] T.J. Williams, *et al.*, Phys.Rev. B **80**, 094501 (2009).

[58] T.J. Williams, *et al.*, Phys. Rev. B **82**, 094512 (2010).

[59] Y. Yin, *et al.*, Phys. Rev. Lett. **102**, 097002 (2009).

[60] M.R. Eskildsen, *et al.*, Phys. Rev. B **79** 100501(R) (2009).

[61] M.R. Eskildsen, *et al.*, Physica C **469** 529 (2009).

[62] L. Ya. Vinnikov, *et al.*, JETP Lett. **90**, 299 (2009).

[63] D.S. Inosov, *et al.*, Phys. Rev. B **81**, 014513 (2010).

[64] L. Luan, *et al.*, Phys. Rev. B **81**, 10051 (2010).

[65] P. Das, *et al.*, Supercond. Sci. Technol. **23**, 054007 (2010).

[66] A. Schenck, Muon Spin Rotation Spectroscopy: *Principles and Applications in Solid State Physics*, Adam Hilger Ltd, England, 1985.

[67] P. Bakule and E. Morenzoni, Contemporary Physics **45**, 203 (2004).

[68] R. Kubo, Hyperfine Interactions **8**, 731 (1981).

[69] R.E. Walstedt and L.R. Walker, Phys. Rev. B. **9**, 4857 (1974).

[70] S.L. Lee, S.H. Kilcoyne, R. Cywinski Muon Science: *Muons in Physics, Chemistry and Materials* SUSSP Publications, Edinburgh, Scotland, 1998.

[71] P.D. de Réotier and A. Yaouanc, J. Phys.: Condens. Matter **4**, 4533 (1992).

[72] A. Abragam, Principle of Nuclear Magnetism, Oxford University Press, London, 1961.

[73] M. Celio, T.M. Riseman, R.F. Kiefl, J.H. Brewer and W.J. Kossler, Physica C **153-155**, 753 (1988).

[74] E.H. Brandt, Phys. Rev. B **37**, 2349 (1988).

[75] J.E. Sonier, J. Phys.: Condens. Matter **22**, 203202 (2010).

[76] J.E. Sonier, Rep. Prog. Phys. **70**, 1717 (2007).

[77] J.E. Sonier, *et al.* Phys. Rev. Lett. **106**, 127002 (2011).

[78] M. Kano, *et al.*, J. Phys. Soc. Jpn. **78**, 084719 (2009).

[79] P. Marsik, *et al.*, Phys. Rev. Lett. **105**, 057001 (2010).

[80] J.-H. Chu, *et al.*, Science **329**, 824 (2010).

[81] J.E. Sonier, *et al.*, Phys. Rev. B **76**, 064522 (2007).

[82] A.S. Sefat, *et al.*, Phys. Rev. Lett. **101**, 117004 (2008).

[83] D. Reefman and H.B. Brom, Physica C **183**, 212 (1991).

[84] M. Kano *et al.*, J. Phys. Soc. Jpn. **78**, 084719 (2009).

[85] P. M. Ossi, Disordered Materials, Springer, New York, 2003.

[86] A. Yaouanc, P. Dalmas de-Réotier and E.H. Brandt, Phys. Rev. B **55**, 11107 (1997).

[87] G.I. Menon, *et al.*, Phys. Rev. Lett. **97**, 177004 (2006).

[88] J.E. Sonier, *et al.*, Proc. Natl. Acad. Sci. USA **107**, 17131 (2010).

[89] S. Komiya, Y. Ando, X.F. Sun, and A.N. Lavrov, Phys. Rev. B **65**, 214535 (2002).

[90] H. Kanai, *et al.*, J. Solid State Chem. **131**, 150 (1997).

[91] Y. Tanabe, T. Adachi, T. Noji and Y. Koike, J. Phys. Soc. Jpn. **74**, 2893 (2005).

[92] M. Oda, T. Nakano, Y. Kamada, M. Ido, Physica C **183**, 234 (1991).

[93] T. Nakano, *et al.*, Phys. Rev. B **49**, 16000 (1994).

[94] M. Hashimoto, *et al.*, Phys. Rev. B **75**, 140503(R) (2007).

[95] S. Wakimoto, *et al.*, Phys. Rev. B **72**, 064521 (2005).

[96] W.A. Hunt, P.M. Singer, A.F. Dederstrom, and T. Imai, Phys. Rev. B **64**, 134545 (2001).

[97] D.E. MacLaughlin *et al.*, Phys. Rev. Lett. **72**, 760 (1994).

[98] M. Celio, Phys. Rev. Lett. **56**, 2720 (1986).

[99] R. Kadono, *et al*, Phys. Rev. B **39**, 23 (1989).

[100] T. Tsuda, *et al*, J. Phys. Soc. Jpn. **57**, 2908 (1988).

[101] D. Bohm and D. Pines, Phys. Rev. **92**, 609 (1953).

[102] Z. Radovic, N. Bozovic, and I. Bozovic, Phys. Rev. B **77**, 092508 (2008).

[103] B. Hitti, *et al.*, Hyperfine Interact. **63**, 287 (1991).

[104] S.B. Sulaiman, *et al.*, Phys. Rev. B **49**, 9879 (1994).

[105] C. Panagopoulos, *et al.*, Phys. Rev. B **66**, 064501 (2002).